

This is the **submitted version** of the journal article:

Lei, Yiming; Ye, Jinhua; García-Antón, Jordi; [et al.]. «Recent advances in the built-in electric-field-assisted photocatalytic dry reforming of methane». Chinese Journal of Catalysis, Vol. 53 (October 2023), p. 72-101. DOI 10.1016/S1872-2067(23)64520-6

This version is available at <https://ddd.uab.cat/record/289775>

under the terms of the  ^{IN}COPYRIGHT license

Recent advances in built-in electric field-assisted photocatalytic dry reforming of methane

Yiming Lei ^{a,b}, Jinhua Ye ^c, Jordi García-Antón ^{b,*}, and Huimin Liu ^{a*}

^a *School of Chemical and Environmental Engineering, Liaoning University of Technology, 121001 Jinzhou, P. R. China*

^b *Departament de Química (Unitat de Química Inorgànica), Facultat de Ciències, Universitat Autònoma de Barcelona (UAB), Cerdanyola del Valles, 08193 Barcelona, Spain*

^c *International Center for Materials Nanoarchitectonics (MANA), National Institute for Materials Science (NIMS), 1-1 Namiki, Tsukuba, 305-0044 Ibaraki, Japan*

*E-mail: liuhuimin08@tsinghua.org.cn (H. Liu)

Jordi.GarciaAnton@uab.es (J. García-Antón)

Highlights

- Mechanism and advantages of photocatalytic dry reforming of methane are summarized.
- Photocatalysts with electric fields for dry reforming of methane are classified.
- The enhancement effects of built-in electric fields are discussed.
- The roles of advanced characterizations and theoretical calculation are introduced.
- Challenges and corresponding strategies are proposed for future in-depth studies.

Abstract: Methane (CH₄) and carbon dioxide (CO₂) are two main greenhouse gases that contribute to global warming. Dry reforming of methane (DRM) is an ideal method to deal with the greenhouse effect because it can react with CH₄ and CO₂ simultaneously and produce syngas. However, conventional DRM technology always requires high thermal energy to trigger the DRM process due to the high energy barrier of CH₄ and CO₂ activation. The development of photocatalysis provides an opportunity for initiating the DRM reaction under mild conditions. Nonetheless, the photocatalytic efficiency is still unsatisfactory, which is attributed to the rapid recombination between photoexcited charge-carrier to a large extent. Constructing a built-in electric field is a promising tactic to overcome this deficiency by enhancing the separation and transfer dynamics of charge-carrier. In this review, the reaction mechanism and thermal catalysts for DRM application are introduced. And the advantages of photocatalytic DRM (PDRM) and potential photocatalysts were summarized. Especially, the recent advances in enhancing PDRM through introducing electric fields via fabricating photocatalysts with ferroelectric effect (ferroelectric-based photocatalysts), heterojunction structures, or localized surface plasmon resonance (LSPR) effect are summarized. Besides, the main and potential effects of advanced *in-situ* characterizations and theoretical calculations are introduced to provide young researchers engaging in the PDRM field with simple guidance. Finally, current challenges and possible strategies in the built-in electric field-assisted PDRM field are proposed, to encourage more in-depth research about this area in the future.

Keywords: Photocatalytic reforming of methane; Electric field; Ferroelectric materials; Heterojunction photocatalysts; LSPR effect

1. Introduction

Dry reforming of methane (DRM) is an attractive strategy to convert greenhouse gas into high-energy-density fuels ($\text{CH}_4 + \text{CO}_2 \rightarrow 2\text{CO} + 2\text{H}_2$, $\Delta G^0_{298\text{K}} = 170.7 \text{ kJ}\cdot\text{mol}^{-1}$).^[1] Nonetheless, both CH_4 and CO_2 are thermodynamically inert nonpolar molecules, meaning high energy input is necessary for dissociating these molecules (e.g. $\sim 440 \text{ kJ mol}^{-1}$ for C–H bond in CH_4 and $\sim 750 \text{ kJ}\cdot\text{mol}^{-1}$ for C=O bond in CO_2).^[2–4] Thus, the current industrial methods for DRM are mainly via thermal catalysis pathway, which always requires high temperatures (800–900 °C) to realize a sufficient CH_4 conversion rate. To reach high temperatures, it is unavoidable to lead to high energy consumption, which in turn results in excessive CO_2 emissions and deactivation of catalysts due to sintering.^[5,6]

Photo energy from solar light irradiation is able to accelerate the activation of CH_4 and CO_2 , favoring uphill reactions.^[7–9] Thus, photocatalytic DRM (PDRM) with solar light as the only input energy source is a promising approach to producing syngas beyond the limitations of a thermal-driven catalytic system.^[10] Generally speaking, the photocatalytic efficiency over a single semiconductor-based photocatalyst is not sufficient for commercialization. Typically, the photocatalytic process can be regarded as three basic steps (**Figure 1a**).^[11,12] Firstly, photocatalysts capture photons from light with a proper wavelength. To excite electrons, the energy of photons should be equal to or higher than the bandgap (E_g) of the semiconductor. The photoexcited electrons populate the conduction band (CB), leaving holes in the valence band (VB). Then, the electrons and holes are separated and transfer to the surface of photocatalysts. Finally, the photogenerated electrons and holes participate in the redox reactions with the reactant absorbed on the active sites at the surface of photocatalysts. During the whole process,

various factors might limit the photocatalytic efficiency, such as a narrow light response range[13–17], poor adsorption/activation of reactants at the catalyst surface as well as high charge separation and transfer resistance.[18–23] Among the above problems, the sluggish separation of photoexcited charge-carrier not only reduces the solar conversion efficiency but also is unfavorable for the subsequent chemical reactions, meaning that enhancing charge transfer dynamics is necessary for improving photocatalytic activity. Hence, it is important to design photocatalysts with intrinsic control over photoinduced charge-carrier dynamics.

Many strategies have been proposed to enhance the transfer dynamics over the photocatalysts. Fabricating catalysts with built-in electric fields is a promising avenue, which includes design of photocatalysts with ferroelectric effect (ferroelectric-based photocatalysts), with heterojunction structures, or with localized surface plasmon resonance (LSPR) effect. Some of these strategies and corresponding types of built-in electric fields include: (1) Photocatalysts with an electrostatic field induced by permanent spontaneous polarization from ferroelectric effect. Ferroelectric material-based photocatalysts (e.g. perovskite) have displayed their great potential for promoting charge transfer behavior, attributed to electric fields induced by the spontaneous polarization (**Figure 1b**).[24,25] (2) Photocatalysts with an interface built-in electric field from heterojunction structures. The construction of type-II heterojunction based on two semiconductors with suitable energy band structure is also a reliable approach through forming a built-in electric field at the interface owing to the staggered gap structure, causing oxidation and reduction processes to be carried out at different semiconductors, separately (**Figure 1c**).[26–28] The type-II heterojunction photocatalysts exclude the disadvantage that reduces the amount of photoexcited charge-carrier due to the external component without

catalytic property. However, one of the inevitable defects in type-II heterojunction photocatalysts is the decline of the redox ability because electrons and holes transfer to the lower conduction band and higher valence band, respectively. To overcome this problem, the Z-scheme heterojunctions have been developed recently. Typically, the Z-scheme charge-carrier transfer pathway can maintain the strong redox abilities of semiconductors because the electrons with stronger reduction abilities and holes with stronger oxidation abilities are preserved, while the charge-carrier with lower redox capacities from heterojunctions will recombine (**Figure 1d**).^[29–32] Therefore, photocatalysts with Z-scheme charge transfer mechanisms have attracted wide attention in various photocatalytic applications. (3) Photocatalysts with a built-in thermoelectric field from LSPR effect. LSPR formed by localized surface plasmon resonating with incident light is also a reliable tactic to improve photocatalytic activity (**Figure 1e**).^[33,34] Metal nanoparticles are suitable candidates to accelerate charge transfer and reactants activation through resonance, which leads to the discontinuous electronic structure in metals and thus constructs a local electric field, between metal nanoparticles and visible-near infrared (Vis-NIR) light. Several studies have indicated that the activity and selectivity of specific products are increased by plasmon-assisted photocatalysis, suggesting the great potential of the LSPR effect for improving photocatalytic (or photothermal catalytic) efficiency.^[35–37]

Many scientific works of photocatalysts with built-in electric fields have been reported in the past several years (**Figure 1f**). From this perspective, some representative works in electric field-assisted PDRM systems will be summarized in this review. The influence and mechanism of ferroelectric effect, type-II/Z-scheme heterojunctions, and LSPR effect in charge transfer

pathway and PDRM efficiency will be discussed. This review will also propose the main challenges and possible solutions of electric field-assisted PDRM to encourage more investigations into this field. Through introducing the recent advances in built-in electric field-assisted photocatalytic DRM, this review article could guide those researchers, who engage in enhancing DRM efficiency or developing photocatalysts with built-in electric fields, so that the development of this crossing area could be promoted.

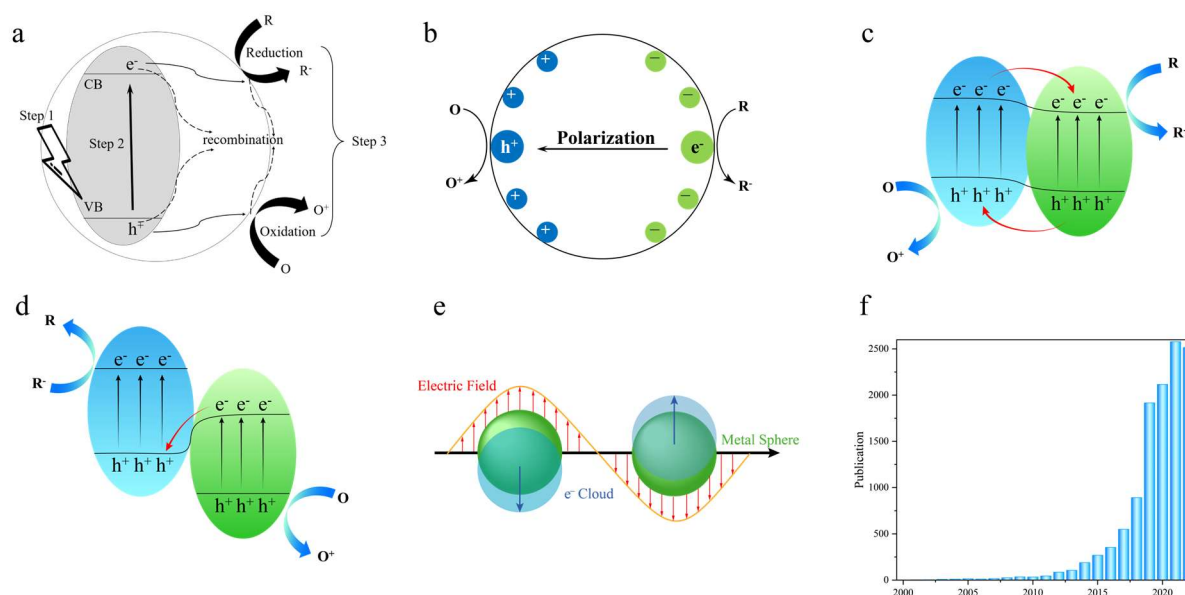


Figure 1. (a) The fundamental steps of the photocatalytic process. Step 1: exciting charge-carrier; Step 2: separation/transfer of electrons and holes; Step 3: reduction and oxidation reactions. (b) Spontaneous polarization in ferroelectric materials induces a built-in electric field that promotes separation and reactions of photoexcited carriers. (c) Type-II heterojunction photocatalyst. (d) Direct Z-scheme heterojunction photocatalyst. (e) Schematic illustration of plasmon oscillation on a plasmonic metal sphere. (f) The publications according to ‘Web of Science’ by searching the keywords ‘photocatalysis’ with ‘electric field’ or ‘heterojunction’ from 2000 to 2022.

2. Fundamentals on dry reforming of methane

2.1. Photocatalytic fundamental mechanism

Typically, photocatalytic reactions always depend on semiconductor-based photocatalysts with suitable energy bands. In terms of energy band structure, as mentioned above, semiconductors generally consist of three parts: VB, CB, and E_g . The VB has low energy, and the CB has relatively high energy. Taking the PDRM reaction as an example, the reaction process can be broadly speaking divided into three steps (Figure 2).

1) Firstly, when an incident light irradiates the semiconductor, if the semiconductor can absorb the incident light and the energy of the photons is greater than (or equal to) the band gap of the semiconductor, then the electrons on the VB can obtain enough energy, leaping to the CB and leaving holes in VB. At the same time, the reactants involving CH_4 and CO_2 are absorbed by the photocatalyst for the subsequent redox reactions (reduction reaction for CO_2 and oxidation reaction for CH_4).

2) The second step is the migration of the photogenerated charge carriers (including electrons and holes) to the photocatalyst surface. However, electrons and holes tend to recombination before they can transfer to the reduction and oxidation sites on the catalyst surface. Thus, too much light energy absorbed by photocatalysts will be wasted instead of participating in chemical reactions. In addition to the photoinduced charge transfer, the reactants will be activated during the second step. But activation is also a difficult and sluggish process in consideration of the thermodynamical stability of both CO_2 and CH_4 non-polar molecules. The details about the dissociation process of CO_2 and CH_4 will be introduced in section 2.2. In brief, the slow activation process also leads to the recombination between photoelectrons and

holes after charge transfers to the photocatalyst surface.

3) After the charge transfer and reactants dissociation processes, the third step involves the reduction reaction of the photoelectrons with electron acceptors (CO₂ molecules) and the oxidation reaction of the holes with the electron donors (CH₄ molecules) over the reduction and oxidation active centers, respectively. Finally, the products of the oxidation and reduction reactions (e.g. CO and H₂) are desorbed from the semiconductor surface to complete the PDRM reduction reaction. Nonetheless, the main problem for the third step is the possible competitive reactions and difficult desorption of products. For instance, the reverse water gas shift (RWGS, Eq. 2-1) reaction often occurs during the DRM reactions, which can influence the selectivity of the products. Besides, the slow desorption of products is able to lead to further interactions (e.g. Eq. 2-2, 2-3), decreasing the product selectivity. More details will be discussed in section 2.5, displaying the current focus on product selectivity from PDRM reaction.

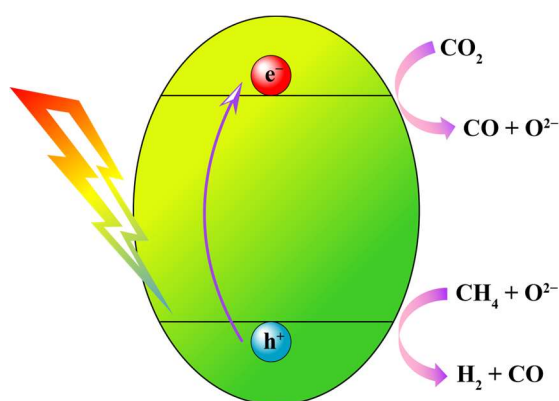


Figure 2 Schematic of PDRM reaction over semiconductor-based photocatalyst.

In addition to the aforementioned deficiencies during three fundamental photocatalytic

steps, many details about the photocatalytic reaction pathways have not been clearly elucidated. In detail, photocatalytic reactions involve a multi-electron transport process, in which the required number of electrons is different due to the various products. Meanwhile, it is difficult to determine the intermediate products, radicals, and other unstable intermediate species by simple characterizations. Therefore, it is difficult to predict the products or clarify the reaction routes.

2.2. Mechanism for dry reforming of methane

DRM has attracted much attention owing to its capacity of converting CO₂ and CH₄ into syngas (CO and H₂ mixture), which can be further utilized as fuels or to produce methanol and butanol.[38] Considering the sufficient reserves of CH₄ and diverse sources of CO₂ like combustion of fossil fuels or agricultural wastes, consuming and re-using these greenhouse gases can meet chemical industrial demand.[39,40] Compared to steam reforming of methane (SMR, Eq. 2-4), DRM has several advantages. Because the water in the feed gas is replaced by CO₂ (Eq. 2-5), less energy is required for the evaporation of water, suggesting the benefit of DRM in energy conversion efficiency.[38] Moreover, the ratio of CO in syngas from DRM (CO : H₂ = 1 : 1) is higher than that from SRM (CO : H₂ = 1 : 3). Therefore, the CO-rich syngas is accessible from DRM, benefiting downstream processes like the synthesis of methanol or other oxo-alcohol products.[41]



Most catalysts activate CH₄ and CO₂ by a bi-functional pathway. Firstly, CH₄ and CO₂ are adsorbed on two different sites. A dehydrogenation process will occur on CH₄ molecules (CH₄

→ CH₃ → CH₂ → CH → C+H, **Figure 3a**). During this process, it is difficult to complete the CH₃-H bond dissociation (which requires an activation energy of 439.3 kJ mol⁻¹), meaning that the activation of CH₄ is one of the rate-limiting steps.[42] For CO₂, it tends to be adsorbed on the surface of a support, metal, or interface (**Figure 3b**). CO₂ can be transformed into CO or carbonate precursors.[43–45] However, due to the thermodynamic stability of CO₂, the dissociation energy of the C=O bond is ~750 kJ·mol⁻¹, indicating that the activation of CO₂ also needs high energy input.[40,46]

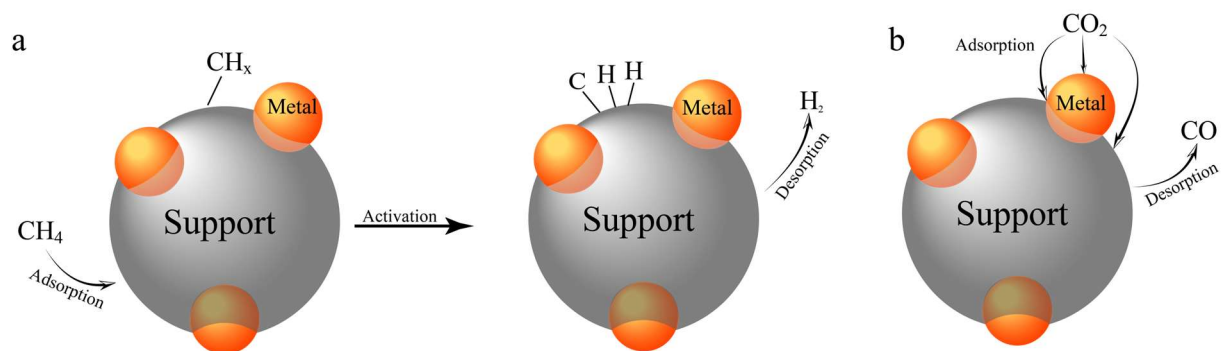


Figure 3. Activation steps of CH₄ and CO₂ for DRM reaction: (a) Dissociative adsorption of CH₄ and desorption of H₂. (b) Adsorption of CO₂ on the metal, metal-support interface and support, and direct formation and desorption of CO.

After activation, the intermediates will react at the metal-support interface. However, the initial activation of CH₄ cannot determine the efficiency of each reaction steps over different catalysts. It is important to construct a kinetic model of the catalysts for improving the catalyst design and being able to predict the intrinsic reaction rates. By assuming different adsorption conditions of reactants (CH₄ and CO₂), three kinetic models including the Power-law, Eley–Rideal (ER), and Langmuir Hinshelwood–Hougen Watson (LHHW) models have been formulated to provide theoretical support for predicting the reaction rates: ① The power-law

model provides necessary parameters with brief estimation but does not consider the reaction mechanism. Thus, this model is regarded as the simplest and roughest approach. Under this assumption condition, more CH_4 than CO_2 is adsorbed on the surface of catalysts and dominates the whole reaction because of the high power constant of CH_4 . ② In ER model, the DRM kinetics is investigated at 700–850 °C and normal pressure ($\text{CH}_4 : \text{CO}_2 = 1 : 1$). Other rate models (e.g. reverse water gas shift reaction, RWGS) are considered as side reactions or competitive reactions.[47] An important assumption is only reactants are adsorbed on the catalyst surface (adsorbed CH_4 or adsorbed CO_2) to interact with other reactants in the gas phase and directly obtain products. The processes of converting methane to hydrogen and active carbon and transforming active carbon with CO_2 to CO are the rate-determining step. Although ER model from Mark et al. contains a complete subset of reactions necessary to describe the network of reactions known to occur under these conditions, the LHHW model due to the conformity of the mechanistic steps in this model proposed with experimental techniques is the most accurate kinetic model for DRM.[47,48] ③ LHHW model assumes that CH_4 and CO_2 can be adsorbed on the catalysts surface simultaneously.[48] During the reaction process, one of the reaction steps is slow and determines the reaction efficiency. The other reaction steps are in thermodynamic equilibrium. The kinetic models from LHHW are constructed according to the dissociative adsorption of two reactants (CH_4 and CO_2) and the conversion of CH_4 and CO_2 to the final products (syngas) through the reaction between CH_x and O . Many studies confirmed that CH_xO is the most abundant reaction intermediates, which can be rapidly dissociated to CO and H_2 . [49] Interestingly, the investigation from Deutschmann revealed that even though there was not any water or steam at the beginning of DRM, water was always observed because of

the RWGS side reaction under thermodynamic conditions.[38] Their work further studied the impact of water on the thermodynamic equilibrium in DRM, which showed that a little steam/water has a slight influence on the ratio of the syngas. Nevertheless, the presence of water promoted the formation of CH_xO , benefiting the evolution of CO and H_2 . In this model, the rate-determining steps include both activation and dissociation processes. Notably, the rate models and expressions are not the focus of this review so that interested audiences are recommended to read references by Schunk and Saché.[38,49]

Selecting catalysts for DRM is another crucial aspect for achieving high conversion efficiency. The cost of catalysts cannot be neglected in this process, but noble metals such as Rh, Ru, Pt, Ir, and Pd have domination due to their excellent activity and good stability at high-temperature conditions.[50–52] An early work was carried out on Ru-loaded Al_2O_3 catalysts ($\text{Ru}/\text{Al}_2\text{O}_3$). The $\text{Ru}/\text{Al}_2\text{O}_3$ catalyst exhibited a 46% conversion rate of CH_4 and 77% selectivity of the H_2 product. Transient kinetic analysis and temporal analysis of products indicated that the whole reforming process occurred in the Ru phase. Al_2O_3 continuously provided the active Ru phase with H and O species, preventing the catalyst deactivation (or Ru oxidation). Furthermore, the activity of Ru supported on La_2O_3 ($\text{Ru}/\text{La}_2\text{O}_3$) toward H_2 generation via DRM has also been investigated by Cornaglia et al.[53] The $\text{Ru}/\text{La}_2\text{O}_3$ catalyst remained stable for more than 80 h in the 823–903 K temperature range with ~15% conversion efficiency of CH_4 . Considering the industrial applications, Ni and Co become candidates for DRM with their high adsorption energy of O and C (**Figure 4a**).[54–56] However, to realize the complete conversion of CH_4 and CO_2 , a high-temperature condition (at least 800°C) is required, which may lead to the sintering and coke of Ni and Co-based catalysts. Recently, bimetallic catalysts (e.g. Rh-Ni,

Pt-Ni, and Pd-Ni) attracted much attention because these catalysts show excellent stability for potential industrial applications for DRM.[57–59] Bimetallic Ni-Pt loaded ZrO_2 catalyst presented higher stability against carbon formation than monometallic Ni/ ZrO_2 . [60] In another example, Rh inhibited the formation of NiO_x via hydrogen spillover so that there was little activity loss after long-term reactions because metallic Ni was maintained (**Figure 4b**). [58] Additionally, Pt and Ru also helped maintain the metallic status of Co during the DRM process, preventing the deactivation from oxidation of Co^0 by CO_2 to inactive $CoTiO_3$ species. [56] Besides the activation and dissociation efficiency, there are several factors affecting the catalytic activity of catalysts in DRM, e.g. reducibility, particle size, surface area, acidity, and basicity. A few reviews summarized the relationships between the above properties and the catalytic behavior of catalysts for DRM, but they focused on the conventional thermo-catalysts and did not pay enough attention to photocatalysts for DRM. [61–63]

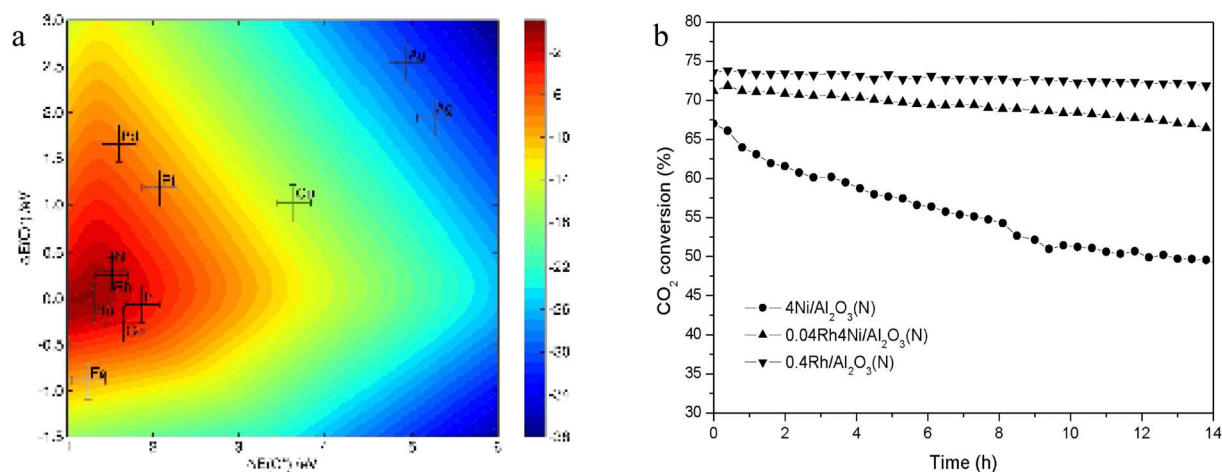


Figure 4. (a) Two-dimensional volcano-curve of the turnover frequency (\log_{10}) as a function of O and C adsorption energy. $T=773$ K, $P=1$ bar; 10% conversion. The error bars include an estimated 0.2 eV uncertainties in the adsorption energies. [64] Copyright 2008, Elsevier. (b) CO_2 conversion vs. time on stream (973 K). [58] Copyright 2011, Elsevier.

2.3. Advantages for photocatalytic dry reforming of methane

For different practical applications, photocatalytic technology always has several advantages, such as strong redox ability, environmental friendliness, low cost, etc. More specifically, the PDRM application has three main benefits as discussed below.

1) Initiating reaction under mild conditions. Because of the high activation energy of both CO_2 and CH_4 , conventional thermal catalysis technology always needs high temperatures to conduct the reforming reaction and avoid inverse reactions. In this case, PDRM is an attractive strategy to decrease these harsh conditions, because the active intermediates could be generated easily via the excitation of photons with high energy through the photon energy. Then, the cleavage of the C–H bond can be achieved at a much lower temperature with a markedly decreased energy barrier.[65] Therefore, photocatalysts are able to carry out thermodynamically unfavorable DRM reactions with solar energy mediation.[66]

2) Solar light as green energy could decrease the consumption of fossil fuels. The conventional industrial catalytic DRM process always needs large consumption of fossil fuel to realize high-temperature, resulting in the excessive emission of CO_2 . On the contrary, photocatalysis utilizes solar light as the only energy source to activate the photocatalyst and drive the oxidation-reduction reaction. This feature makes photocatalysis more attractive from an energy point of view.[67,68]

3) Safety and long longevity. The mild reaction conditions provide advantages of safety. For instance, compared with more than $800\text{ }^\circ\text{C}$ for thermal catalytic DRM reaction, PDRM only needs reaction temperatures below $500\text{ }^\circ\text{C}$, meaning fewer safety hazards.[65,69] What's more, owing to the low-temperature, more photocatalysts could be selected for DRM application. And

the catalyst sintering, which is always observed at high-temperature during thermal catalysis, could be avoided to a large extent, extending the longevity of catalysts.[70]

2.4. Potentials photocatalysts for dry reforming of methane

Before the exhaustive introduction of the built-in electric field-assisted photocatalytic systems for DRM application, photocatalysts most likely to be used for DRM reactions are summarized in this section. And the current challenges and corresponding solutions of these photocatalysts will also be displayed. Briefly, they could be divided into semiconductor and non-semiconductor materials.

2.4.1. Semiconductor photocatalysts

1) **Metal oxides.** Most semiconductor materials belong to metal oxides, such as TiO_2 , WO_3 , and ZnO . Among them, TiO_2 is a suitable candidate owing to its wide range of applications. Since 1972, TiO_2 was reported as a photo(electro)catalyst by Fujishima and Honda,[71] all the photocatalytic applications like water splitting, CO_2 reduction, and organic pollutants degradation could be achieved by different types of TiO_2 photocatalysts. Thus PDRM is no exception. However, the two greatest problems of TiO_2 for efficient syngas production are narrow light response range and rapid photoinduced charge recombination. Much research has been done for enhancing the PDRM efficiency of TiO_2 . For instance, Miyauchi et al. synthesized a monoclinic-phase TiO_2 -B nanobelts-supported rhodium (Rh/TiO_2 -B nanobelts) photocatalyst.[72] The low enough VB of TiO_2 enabled photoexcited holes to take part in CH_4 oxidation, while the photoelectrons were trapped in Rh to reduce CO_2 (**Figure 5a**). Thus, Rh/TiO_2 -B could fully use the light energy to exceed the equilibrium-limited performance of the thermal catalytic DRM system for syngas production. The production rates of H_2 and CO_2

over Rh/TiO₂-B were 21.5 and 21.2 mmol·h⁻¹·g⁻¹, separately. Besides loading co-catalyst, another promising strategy is the fabrication of black TiO₂ with oxygen deficiency. Since 2011, Chen et al. obtained black TiO₂ by hydrogenation treatment, black TiO₂ has obtained much attention from different photocatalytic application fields because of its unique electronic and optical properties. However, in the PDRM area, only a few works about black TiO₂ were reported. Han's group reported an efficient visible-light photocatalytic CH₄ reforming with CO₂ by combining Pt/black TiO₂ catalyst with a light-diffuse-reflection surface.[73] H₂ and CO yields could reach 71 and 158 mmol·h⁻¹·g_{cat}⁻¹ under AM 1.5 light illumination without UV light. This work focused on the practical DRM application over black TiO₂ because the process exhibited high apparent quantum efficiencies of 32.3% at 550 °C and 57.8% at 650 °C for the entire visible light range (**Figure 5b**). Therefore, it confirmed that black TiO₂ is an excellent candidate for the future industrialization of PDRM technology. At present, the main challenge focuses on the lack of reliable methods for the large-scale synthesis of black TiO₂, which should be fully given adequate attention in future works.

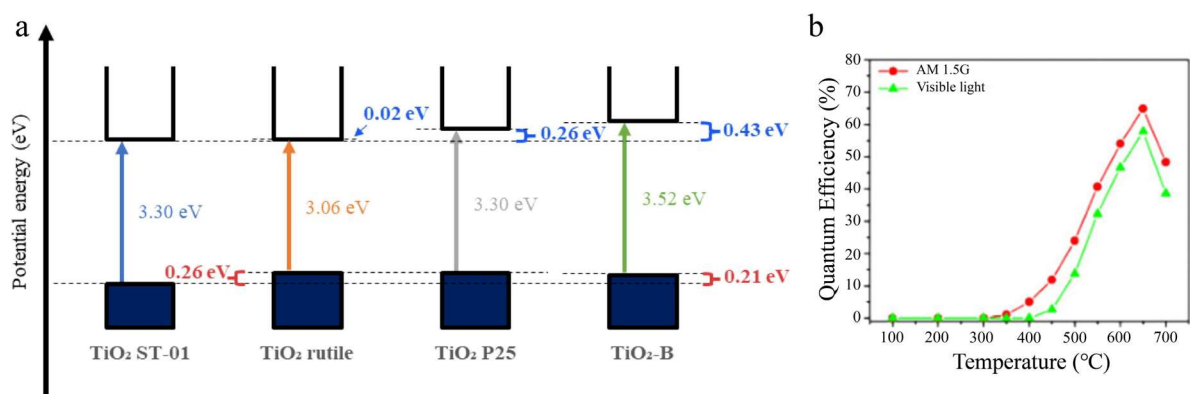


Figure 5 (a) Energy band structure of various TiO₂ samples. Here, the band structure is drawn with respect to the top edge of VB of TiO₂ ST-01 for relative comparison.[72] Copyright 2022, ELSEVIER. (b) Quantum efficiency (QE) versus temperature (*T*).[73] Copyright 2016,

American Chemical Society.

In addition to TiO₂, there are some investigations about WO₃, ZnO, and other semiconductors for PDRM. And all of them displayed promising potential in the selectivity, efficiency, and stability perspectives, suggesting that metal oxides-based photocatalysts should be furtherly explored for the industrialization of DRM as soon as possible. Inevitably, all the single metal oxides-based photocatalysts have the same challenges as the aforementioned TiO₂ photocatalysts. Fortunately, many efforts have been made to improve their photocatalytic activity, especially in the PDRM area. Some review articles have systematically summarized general strategies including loading co-catalysts, dye sensitization, elemental doping, etc. Interested readers are recommended to read ref. [74–76]. In this review article, more attention will be paid to the role of constructing built-in electric fields in photocatalysts and clarify the mechanism of the electric fields during PDRM reaction via introducing recent or typical works.

2) **Carbides and nitrides.** The majority of carbides used for DRM could be considered as MXene materials. It cannot be denied that this kind of 2D carbon-based materials indeed show outstanding ability in different photocatalytic areas (e.g. water splitting, methane conversion, and even ammonia synthesis). For DRM application, multilayer vanadium carbide MXene with Ni substance (m-V₂C/Ni) has been used under the 800 °C thermal catalytic condition.[77] The optimal CH₄ and CO₂ conversions were 94% and 89%, respectively. And the stability of the m-V₂C/Ni catalyst could maintain for more than 90 h. But for PDRM, due to the limitation of their energy band structure (the narrow E_g), most of them have to combine with other semiconductors with wide E_g to achieve the strong optical property and efficient charge separation while obtaining strong redox capacity for photocatalytic reactions. In this regard, Khan et al. reported

lots of works about Ti_3C_2 MXene coupled with different semiconductors like anatase/rutile TiO_2 and $\text{g-C}_3\text{N}_4$, forming heterojunctions and realizing CH_4 reforming with CO_2 . [78–81] All of these studies revealed that the unique 2D structure and excellent electronic conductivity of Ti_3C_2 were beneficial for the PDRM process. Considering that more functionalization methods of MXene were developed, it could be expected that MXene/semiconductor composites have great potential for PDRM technology.

A series of nitrides (e.g. GaN , $\text{g-C}_3\text{N}_4$) have been reported that they possessed excellent activity and good selectivity during PDRM reactions. $\text{g-C}_3\text{N}_4$ as the most popular and widely studied polymeric nitrides were gradually investigated in the PDRM field. For example, 2D/2D porous $\text{g-C}_3\text{N}_4$ -GO nanocomposite was fabricated by Tahir's group, exhibiting $399 \mu\text{mol g}^{-1}$ for CO evolution after 4 h photocatalytic reactions. [82] The authors claimed that the GO nanosheet had an electronic conductive channel for electron-hole pairs transfer, enhancing the DRM activity of $\text{g-C}_3\text{N}_4$. However, the evolution rate of H_2 was much lower than that of CO , seemingly suggesting that the selectivity should be adjusted and optimized in future in-depth studies. Unfortunately, besides the research from Tahir's group, other works about nitrides and carbides for PDRM also had a similar deficiency. Hence, it is necessary to fully govern the selectivity during the PDRM process as discussed below.

2.4.2. non-semiconductor photocatalysts

Because there is no photoexcited charge-carrier from non-semiconductor, plasmonic metals are the most common non-semiconductor photocatalysts for photocatalytic CH_4 conversion reactions. Upon focused illumination, the surface temperature of plasmonic metal nanoparticles is raised to an equilibrium temperature (T_{eq}) owing to the photothermal

conversion caused by the strong absorption and the IR heating effect of focused illumination. Once T_{eq} exceeds the light-off temperature ($T_{\text{light-off}}$) of thermocatalytic DRM, the DRM reaction proceeds. Currently, noble metals and transition metals, such as Au, Ni, and Cu, have been widely utilized for PDRM applications.[81] For instance, a photothermal catalyst with a plasmonic Pt active component and CeO₂ substrate is a potential candidate for PDRM. Mao's group designed Pt/CeO₂ nanorods. It displayed high evolution rates for both H₂ and CO (5.7 and 6.0 mmol·min⁻¹·g⁻¹, **Figure 6a**) and even a high light-to-fuel efficiency (η , 10.3%, **Figure 6b**).[83] More importantly, the diffusive reflectance absorption spectrum of Pt/CeO₂ has a strong broad absorption from ~425 to 2400 nm, corresponding to the surface plasmon resonance (SPR) of Pt nanoparticles (**Figure 6c**). Thus, the authors believed that the high activity should be attributed to the solar-light-driven thermocatalytic process, which was achieved by the hot electrons with high energy induced by light illumination. The further *in-situ* FTIR and isotope labeling results studied the cooperation between Pt and CeO₂. And the results suggested that mesoporous CeO₂ made the interface oxygen more active due to the metal–support interaction, causing a reverse oxygen spillover to the surface of Pt nanoparticles. This oxygen spillover participated in the dissociation of CH₄ to CH_x species on Pt. Meanwhile, the oxygen vacancies accelerated the dissociation of CO₂ molecules. And the chemisorbed oxygen from CO₂ activation could replenish the oxygen vacancies via oxygen spillover. Thus, the synergistic effect improved the PDRM reaction efficiency and durability of Pt/CeO₂ simultaneously.

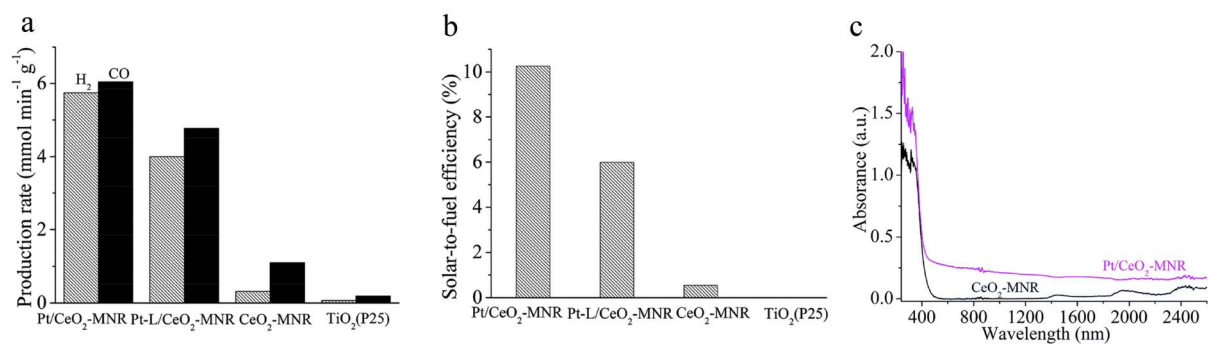


Figure 6 (a) Production rate (b) and light-to-fuel efficiency of the catalysts for CRM under the focused irradiation of full solar spectrum light from the Xe lamp. (c) Diffusive reflectance absorption spectra of Pt/CeO₂-MNR.[83] Copyright 2018, Royal Society of Chemistry.

Besides the hot electrons of metal nanoparticles participating in the PDRM process, another important effect of plasmonic metal nanoparticles is their localized surface plasmon resonance (LSPR) effect, which could form a strong electric field at the interface between metal nanoparticles and the substrate. Recently, the LSPR effect has been widely used in the photothermal catalytic DRM field, thus more details about how to verify its role and some representative works will be introduced in section 5.

2.5. Photocatalytic selectivity for dry reforming of methane

Some CH₄ conversion applications (e.g. steam reforming of methane, partial oxidation of methane, and oxidative coupling of methane) can lead to oxygenated products like methanol and formaldehyde with more reactive properties than CH₄, and thus easily producing undesired products and resulting in poor selectivity.[84–86] In addition to the oxidation products, reactive oxygen species ([•]OH) is also able to oxidize products so that reducing undesired products is still a big challenge for chemical transformation.[65] When talking about the selectivity during the PDRM reaction, the main works mainly focus on adjusting the ratio between CO and H₂ and

inhibiting some undesired reactions, which can form carbon deposition (Eq. 2-6, 2-7). Thus, one strategy to control the selectivity is to decrease the carbon deposition, enhancing the catalyst stability. From this perspective, designing catalysts with unique morphology is an effective method.[87] Core/yolk-shell structures have been widely used for preventing the sintering of active metal cores surrounded by metal oxide shells, thereby improving catalytic stability.[88–90] And constructing porous surfaces on catalysts is also a reliable method because high porosity is able to reduce the mass transfer barrier and increase the accessibility of the active sites by reactants, thus leading to high catalytic activity.[91,92] A recent work about using core-shell structure to adjust the selectivity of CO₂ photoreduction was reported by Lee et al.[93] In this work, the authors utilized hydrothermal treatment to synthesize Cu-Ni bimetallic cocatalyst and loaded it onto the CN nanosheet via the impregnation method. EDX results clearly revealed the core-shell structure of Cu-Ni nanoparticles with the inner Cu core (~30 nm diameter) and Ni shell (10 nm thickness, **Figure 7a–d**). And the Cu-Ni also resulted in the enhancement of the light absorption ability of Cu-Ni@CN due to the surface plasmon resonance (SPR) effect of Cu. Under visible light illumination, the optimal CH₄ production rate of 75.2 μmol h⁻¹ g⁻¹ was achieved by Cu–Ni-11@CN catalyst (Cu: Ni molar ratio = 1:1, **Figure 7e**). And the maximum selectivity for CO₂ reduction was ~ 97% over Cu–Ni-13@CN catalyst. The improved selectivity should be attributed to the core-shell structure since more CO as a competitive product was produced by Cu@CN and Ni@CN catalysts without unique morphology. And the core-shell structure also caused good stability so that Cu–Ni@CN catalyst could maintain a high CH₄ evolution rate after several CO₂ photoreduction cycles (**Figure 7f**).

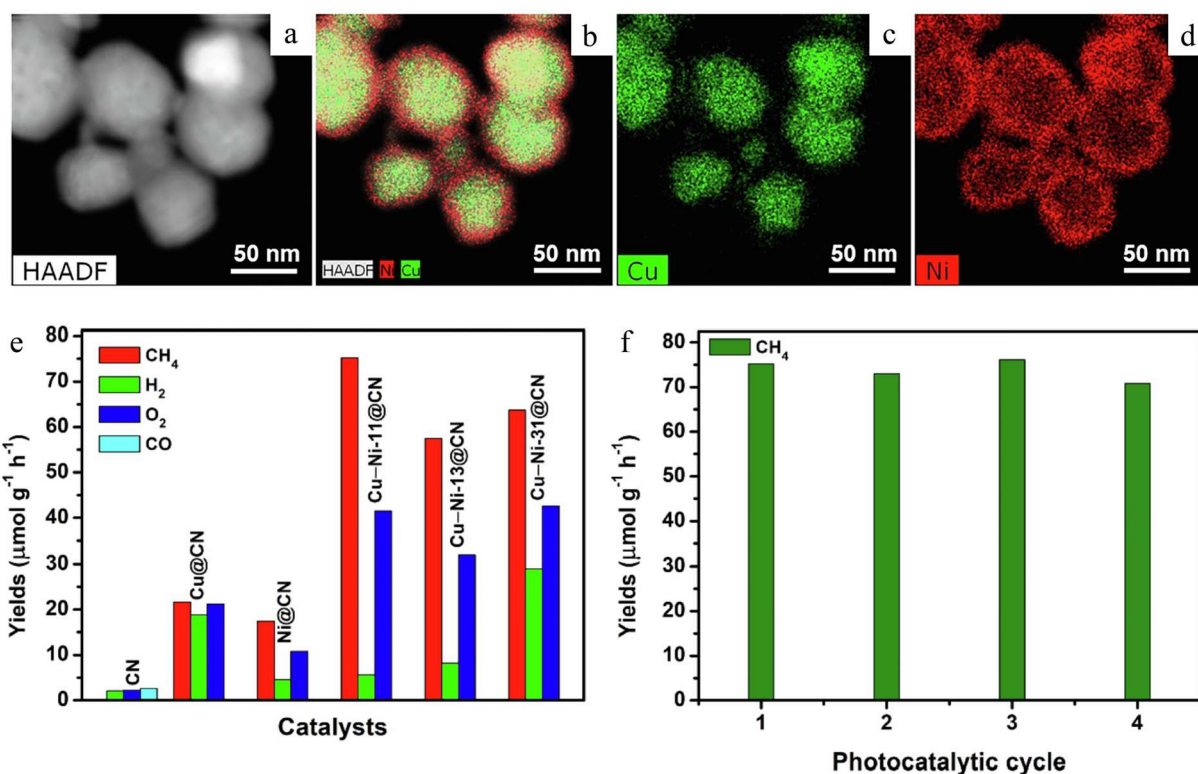


Figure 7 (a–d) HAADF-STEM elemental distribution maps of the Cu–Ni-11@CN catalyst. (e) Comparison of the amount of CO₂ reduction products over the synthesized catalysts upon 5 h of light irradiation. (f) Reusability tests of CH₄ generation over the Cu–Ni-11@CN catalyst.[93]
Copyright 2022 Elsevier B.V.



Another focus for adjusting the product selectivity is governing the ratio of H₂ and CO during the syngas production process. Here we take Rather's work as an interesting example.[94] In this work, the authors prepared graphitic carbon nitride nanotubes modified with lanthanum (La/g-CNT) for dynamic photocatalytic CH₄ conversion with CO₂, displaying 491 μmol·g⁻¹·h⁻¹ evolution rate for CO, which is 5.9 folds higher than that of pure g-C₃N₄ sample. But the most important idea in this work was CH₄/CO₂ feed ratios could obviously adjust the CO and

H₂ yield rates, respectively. In detail, the highest CO was produced at CH₄/CO₂ = 1.0. On the contrary, the maximum evolution efficiency of H₂ was achieved with a ratio of 2.0. The discussion on reaction mechanism clarified the relationship between selectivity and reaction pathway. After CH₄ was oxidized by h⁺ and CO₂ consumed by e⁻ (Eq. 2-8), CO₂^{·-} as intermediate might react with H⁺, forming CO and H₂O (Eq. 2-9, 2-10). In this case, CH₄ could be oxidized by OH⁻ radicals from H₂O oxidation. Meanwhile, the presence of H₂ (from H₂O splitting, Eq. 2-11, 2-12) also caused the RWGS reaction, furtherly leading to the high evolution of CO (Eq. 2-13). Thus, the selectivity was so sensitive to the ratio of CH₄/CO₂.



Product selectivity is often overlooked when evaluating the properties of DRM catalysts. However, for a practical and industrial application, a catalyst must achieve high activity, stability, and excellent selectivity towards syngas products.[95] Considering the detrimental effects such as carbon formation, catalyst deactivation, and product consumption, the balance between activity and selectivity should gain enough attention in future works.

2.6. Photothermal effects for dry reforming of methane

Photothermal catalysis is able to utilize the advantages of thermal catalysis and photocatalysis to obtain excellent catalytic efficiency under moderate conditions. Based on the

mechanism that triggers chemical reactions, photothermal catalysis can be classified into three types.

1) Thermal-assisted photocatalytic reaction. The essence of thermal-assisted photocatalysis is the photochemical reaction route. It means that the desired chemical reaction cannot be carried out only by heating without light illumination.[96] Therefore, the role of thermal energy is assisting, reducing the activation energy of photocatalysis and promoting charge and molecule transfer.

2) Photo-assisted thermal catalysis. For the second type, the chemical reaction mechanism should be considered as a thermochemical process.[97] In this case, light irradiation is the heating source, exciting vibrational states. And the effect of photochemistry is slight. Thus, photo-assisted thermal catalytic systems always need some photothermal catalysts with strong and wide light absorption ability and light-to-thermal conversion efficiency so that more solar light could be absorbed for providing catalysts and reactants with energy,[98] overcoming the harsh conditions during the conventional thermal reactions.[99]

3) Photothermal synergistic catalysis. The third type is photothermal co-catalysis, in which the photochemical and thermochemical pathways are coexistence. In brief, the thermal energy from the photothermal effect could promote the chemical reactions via thermochemical routes, and the photoexcited charges also benefit the activity.[100] Therefore, photothermal synergistic catalysis couples the excited electronic states or hot carriers with the excited vibrational states of photocatalysts.

According to the above classification, the key to distinguishing between photocatalysis and photothermal catalysis is whether photogenerated charges are excited and directly

participate in catalytic reactions. Besides, photothermal catalysis could also be classified by different interaction mechanisms of light and catalysts, involving plasmonic localized heating, non-radiative relaxation in semiconductors, and thermal vibration of molecules. Ma et al. have well-summarized their differences, and interested readers could read ref. [101].

One of the photothermal catalytic systems often used in the PDRM field is photo-assisted thermal catalysis, which introduces an external light source during the thermal catalytic process and thus initiates redox reactions under mild reaction conditions. Recently, Yang's group loaded Ni half-metal clusters onto an Al₂O₃ substrate (hm-Ni/Al₂O₃) for a light-driven DRM reaction.[102] The UV-vis spectra exhibited the high absorption capacity of hm-Ni/Al₂O₃ across entire solar spectra from 240 to 2400 nm (**Figure 8a**). The strong optical properties should be attributed to the narrow energy gap of ~ 0.3 eV. During photothermal DRM experiments, single Al₂O₃ had almost no activity (**Figure 8b**), meaning that this system should be considered as photo-assisted thermal catalysis as mentioned above. On the contrary, the H₂ and CO evolution rates over hm-Ni/Al₂O₃ could achieve 8572.96 and 9614.26 mmol·min⁻¹·g_{Ni}⁻¹, which are more than one order of magnitude higher than those of Ni nanoparticle loaded-Al₂O₃ catalyst. Compared with the photocatalytic activation process over semiconductor-based photocatalysts, which could generate reactive oxygen species for CH₄ dissociation, the CH₄ activation processes during photo-assisted thermal catalysis depends on the formation of energetic hot carriers from the excitation of surface plasmons over metal nanoparticles.[103–105] The hot carriers inject from the metal surface to the accessible orbitals of reactants (CO₂ and CH₄). Another activation method is the interaction between metal nanoparticles and the absorbates, causing the hybridized electronic states, which can realize the direct charge transfer for

activating reactant molecules. What's more, the plasmon excitation also constructs an interface electric field,[106,107] which can adjust the charge distribution in CH₄ molecules so that the adsorption and dissociation of CH₄ could be promoted.[108] In brief, the direct carrier transfer mechanism and electric fields from the photothermal effect are beneficial for accelerating the first step during the PDRM process, and thus improving the subsequent redox reactions. In this review article, the role of the electric field induced by plasmonic metal nanoparticles and classical works to identify the above enhancement effect during the photothermal DRM process will be summarized in section 5.

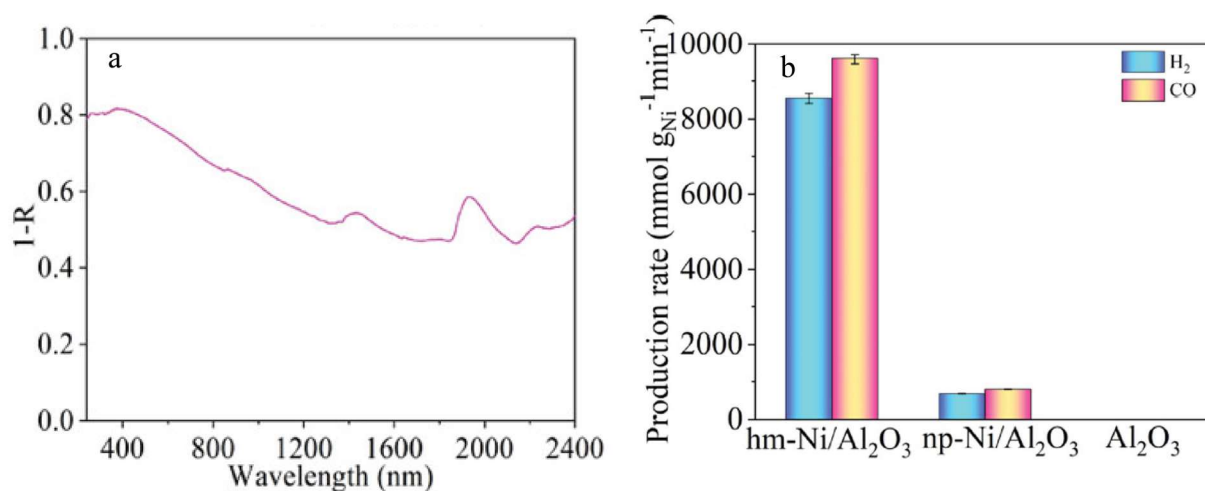


Figure 8 (a) Diffusive reflectance spectrum of hm-Ni/Al₂O₃. (b) The specific production rates of H₂ and CO for light-driven catalytic DRM on the samples under concentrated UV–vis–IR illumination with a light intensity of 345.6 kW·m⁻². [102] Copyright 2023 Wiley.

2.7. Advantages and disadvantages of built-in electric field-assisted photocatalytic dry reforming of methane

In addition to the above benefits of photo(thermal)catalysis for DRM reaction, other unique advantages of built-in electric field-assisted PDRM systems should be mainly attributed to their electric field.

1) Enhanced charge transfer kinetics.[109] Undoubtedly, the most direct impact of electric fields in photocatalysts is the accelerated charge migration process. Although the excitation process of photoinduced charge-carrier is rapid, the large charge transfer resistance of conventional semiconductor-based photocatalysts greatly limits the subsequent transportation of photoexcited charges. In this case, the regular distribution of positive and negative potentials owing to the polarization, charge diffusion, and concentration difference at the heterojunction interface, or hot-excited charge vibration could promote the charge transfer. And the construction of an electric field also inhibits the recombination between electrons and holes via the Coulomb force.

2) Separated reduction and oxidation active sites. After the separation of charges, the subsequent redox reactions are also benefited from the built-in electric fields, since photoelectrons and holes have been accumulated on different sites over photocatalysts. Thus, it could be expected that some undesired reactions like reverse reactions during the PDRM process could be inhibited because reduction and oxidation products are separated to different sites, too. After they complete the desorption process, it is difficult for them to re-occupy the active centers and carry out the reverse process.

For disadvantage, it is also from the built-in electric field. In detail, these electric fields are static so that it is easily to be saturated by the inner and outer shielding effects from photoinduced carriers, charged-free carriers, and radicals.[110,111] This defect decreases the positive influence of the built-in electric field, thus limiting the photocatalytic performance. Although this deficiency cannot be ignored, the built-in electric field-assisted photocatalysts have displayed great potential in not only the PDRM area but also other photocatalytic

applications. Thus, it is necessary to summarize the advances in this field to drive more investigations so that the above problems could be overcome with increasing research.

3. Photocatalysts with ferroelectric field from ferroelectric effect

Photocatalytic processes exhibit a great capacity for reducing energy barriers and realizing high activity without programmed heating equipment contained in conventional thermal-driven reaction vessels.[112] It means that the activation of CH₄ and CO₂ molecules is not the biggest inhibition for improving the conversion rate of CH₄. In this case, another challenge, the high probability of charge-carrier recombination, becomes the main problem for efficient DRM.[13] Actually, thermal energy is a double-edged sword for photocatalytic (or photothermal catalytic) activity. High temperatures led by external heating or light illumination on one hand undoubtedly accelerate the random motion of molecules, while on the other hand, it increases the recombination rate of electrons and holes and further leads to the loss of input energy, limiting the whole photocatalytic efficiency.[113,114] To deal with this great problem, ferroelectric-assisted photocatalysis has obtained wide attention in recent years.

Ferroelectric materials are polar noncentrosymmetric (NCS) materials with domain walls that can generate an electric field when the positive-negative charge centers do not coincide. In detail, owing to the non-centrosymmetric crystal structure of ferroelectrics, ferroelectric materials possess spontaneous polarization without external stimulation. [115–120] The direction of the polarization can be reversed or redirected by an external electric field. However, high-temperature conditions (called Curie temperature, T_c) will make ferroelectric materials lose their ferroelectricity because their crystal structure is symmetrical at high temperatures. Among the three types of ferroelectric materials (Rochelle salt, KDP (KH₂PO₄), and perovskite),

perovskite always has high intensity of spontaneous polarization and photoelectric effect simultaneously.[121–123] Thus, some conventional perovskite-based catalysts have been further developed in the DRM field due to their intrinsic ferroelectric property. For instance, Chung’s group proposed $\text{BaZr}_{0.05}\text{Ti}_{0.95}\text{O}_3$ (BZT) catalyst and focused on the benefits of the ferroelectric effect to a large extent.[124] The external electric force enabled the opposite movement of anions and cations. When the external electric field was off, the BZT catalyst could maintain the status of polarization, increasing the dynamics of charge-carrier and further leading to the separation of photoelectrons and holes (Figure 9). The cooperation between the plasma assistance and the built-in electric field induced by the ferroelectric property increased the charge density, leading to 79.0% conversion of CO_2 and 84.2% conversion of CH_4 .

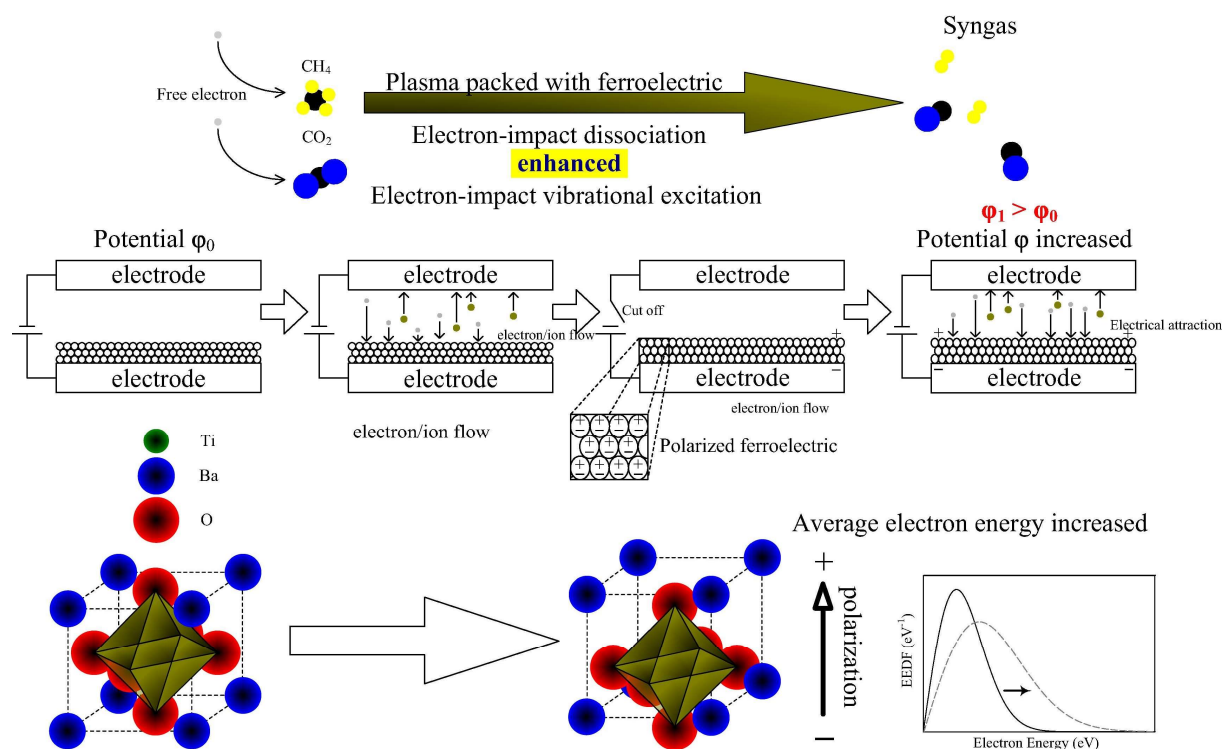


Figure 9. Mechanism of ferroelectric polarization and its effect on dry reforming.[124]

Copyright 2016, Elsevier.

For the PDRM field, Karamian et al. reported a BaTiO_3 photocatalyst with Fe_2O_3 loading

(BF) for CO₂ photoreduction in the presence of CH₄, which could be regarded as a PDRM reaction.[125] According to photoluminescence (PL) signals, BaTiO₃ exhibited the least rate of charge recombination because of its intrinsic ferroelectric property, which could suppress charge recombination (**Figure 10a**). Another result from PL spectra was the heterojunction structure of BF, meaning that photoexcited electrons and holes transfer across the interface of the two components. Thus, with the increasing amount of BaTiO₃, the BF41 (41 denoted the molar ratio of BaTiO₃ to Fe₂O₃) composite possessed the most effective charge transfer behavior, suggesting the important role of BaTiO₃ as ferroelectrics in charge transfer dynamics. During PDRM experiments, under visible light irradiation ($\lambda > 400$ nm), the CO₂ conversion rate was increased from 9.4% on BaTiO₃ to 22.3% on the BF31 sample (**Figure 10b**). To confirm the role of a heterojunction structure in enhancing charge transfer, the photocatalytic activity of a physical mixture of BaTiO₃ and Fe₂O₃ was evaluated, in which the activity was much lower than that in BF heterojunctions (**Figure 10c**). Thus, the considerable performance of BF heterojunctions suggested the synergistic effect from the ferroelectric effect, excellent interfacial structure, and active sites. Notably, both BaTiO₃ and Fe₂O₃ are n-type semiconductors, thus the possibility of enhancement from p-n heterojunction was excluded. Furtherly, since the Fermi levels of BaTiO₃ and Fe₂O₃ are close to the CB, the equilibrium of Fermi levels had no obvious effect on their band structures. It is undeniable that this work focused on the function of ferroelectric materials and eliminates other probable enhancement mechanisms via systematic characterization. Hence, it has reference significance for future works.

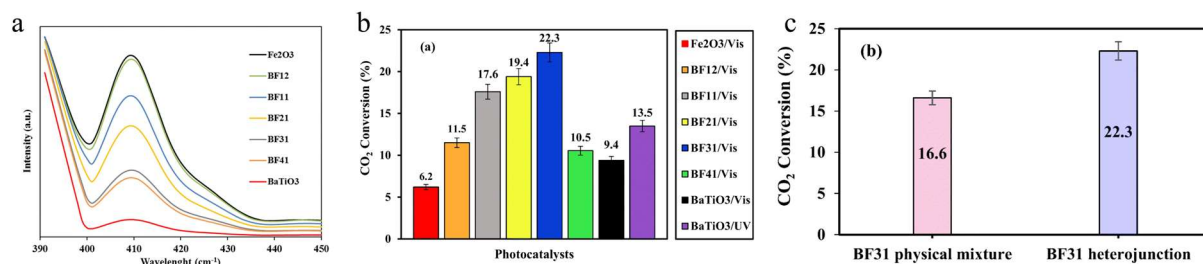


Figure 10. (a) The PL spectra of BaTiO₃, Fe₂O₃, and different molar ratios of BaTiO₃-Fe₂O₃. (b) The efficiency of different photocatalysts used for CO₂ reduction within 4 h. (c) A comparison between the photocatalytic performance of BF31 heterojunction and physical mixture of BaTiO₃ and Fe₂O₃ with the same molar ratio. [125] Copyright 2019, Springer Nature.

Liu et al. reported TaN ferroelectric material as photocatalyst support for photo-assisted CO₂ reduction with methane. [126] Pt was loaded on TaN and Ta₂O₅ by a wetness impregnation method to prepare Pt/TaN and Pt/Ta₂O₅ photocatalysts. Both Pt/TaN and Pt/Ta₂O₅ were effective for CO₂ and CH₄ conversion at 500 °C without light irradiation. However, with visible light irradiation, only the photocatalytic activity of Pt/TaN was improved, suggesting that TaN is an excellent optical material for enhancing photocatalytic activity. The convergent beam electron diffraction (CBED) method of TEM indicated that TaN had polarity, which could induce an electrostatic field (**Figure 11a**). Thus, the electron-hole separation and transfer would be facilitated by a built-in electric field, preferentially participating in CO₂ and CH₄ conversion. On the contrary, the photocatalytic activity over TiN- or ZrN-based catalysts had no obvious enhancement under visible-light illumination because both TiN and ZrN did not have a ferroelectric effect (**Figure 11b and c**). Thus, the electrostatic field over TaN was important in enhancing the activities with visible light irradiation.

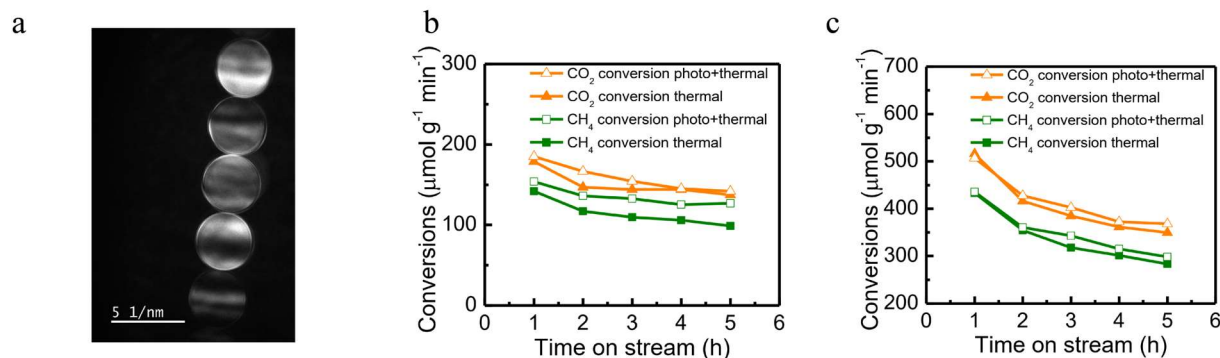


Figure 11. (a) CBED pattern of TaN giving asymmetric contrast between (0001) and (000 $\bar{1}$) diffraction spots. It indicates a polarity of (0001) plane for non-symmetric crystal structure like TaN with space group P-62m. Catalytic performance of (b) Pt/ZrN and (c) Pt/TiN in DRM under different reaction conditions.[126] Copyright 2018, Wiley.

In addition to directly facilitating the charge transfer, the adsorption of reactants at specific active sites can also cause band bending due to the different intermediates and charge accumulating on the polar surface.[127] The direction of bending depends on the polarity of the surface-bound charges. In detail, for the negative polarity surface (or active sites), electrons are depleted leading to a depletion layer with upward band bending, which restricts the photoelectrons transfer but drives the movement of holes towards the surface.[128,129] On the contrary, electrons are accumulated on the surface with positive polarity to form an accumulation layer with downward band bending, which favors the continuous flowing of electrons from ferroelectric photocatalysts to reactants.[130,131] Another important function of ferroelectric-based materials is providing highly dense surface active sites. The positive polarization state is beneficial for electrons transfer to activate CO₂ into $\cdot\text{CO}_2^-$ bidentate radical. After activation, and through an electron-coupled proton transfer mechanism, $\cdot\text{CO}_2^-$ can be converted to $\cdot\text{HCOO}^-$, and then HCOOH can be generated with the addition of H⁺.[132]

Accordingly, it can be inferred that the negative polarization surface would lead to the rapid dissociation and dehydrogenation of CH₄, indicating that the oxidation and reduction reaction processes are carried out at different sites of the ferroelectric materials, separately. Therefore, due to the enhanced charge transfer dynamics and promoted activation of reactants, electrons and holes tend to participate in the redox reactions instead of recombination. All these promising physical properties of ferroelectric materials provide favorable conditions for diverse photocatalytic applications. Actually, more and more ferroelectric materials have been utilized for CH₄ conversion.[10,133] However, to a large extent, many works did not investigate the influence of the ferroelectric effect on charge separation efficiency but simply attributed the improvement of PDRM efficiency to the role of cocatalysts or energy band tuning. Although some authors might speculate that such high temperature from light irradiation during photocatalytic (or photothermal catalytic) reactions might weaken or eliminate the ferroelectric property, the Curie temperature (T_c) of ferroelectric materials (e.g. BiFeO₃ with T_c ~ 825 °C) is higher than the necessary temperature of CH₄ conversion so that the ferroelectric characteristic will not be eliminated while using them for photothermal DRM, meaning that the role of ferroelectric effect must be thought carefully in a PDRM system containing ferroelectrics.[132] Thus, we would like to see more in-depth research on the relationship between the ferroelectric effect and PDRM performance in the future.

4. Photocatalysts with heterojunction structures

The heterojunction is defined as an interface between two different semiconductors with unequal band structure, leading to band alignments.[134] There are three types of conventional heterojunction structures, denoted as type-I, type-II, and type-III heterojunctions, respectively.

For type-I heterojunction photocatalysts, the CB and VB of semiconductor I (SI) are higher and lower than that of semiconductor II (SII), separately (**Figure 12a**). Thus, type-I heterojunction photocatalysts have straddling gap structure.[135] In type-I heterojunction, the photoexcited charge will accumulate at SII, causing that electron-hole pairs cannot effectively separate. For type-II heterojunction photocatalysts with a staggered gap, SI has higher CB and VB than SII, meaning that electrons will migrate to the CB of SII, whereas photogenerated holes will transfer from SII to SI (**Figure 12b**).[136,137] Therefore, the charge recombination is reduced by type-II heterojunction photocatalysts. The architecture of the type-III heterojunction photocatalyst has a broken gap structure that the bandgaps do not overlap (**Figure 12c**).[138,139] Therefore, type-III heterojunction is not suitable for enhancing charge transfer dynamics. Obviously, the type-II heterojunction is beneficial for spatial separation of photoelectrons and holes and thus improves photocatalytic activity compared to other heterojunctions. In the past decades, tremendous efforts have been made to increase photocatalytic efficiency by type-II heterojunction photocatalysts.[140–142]

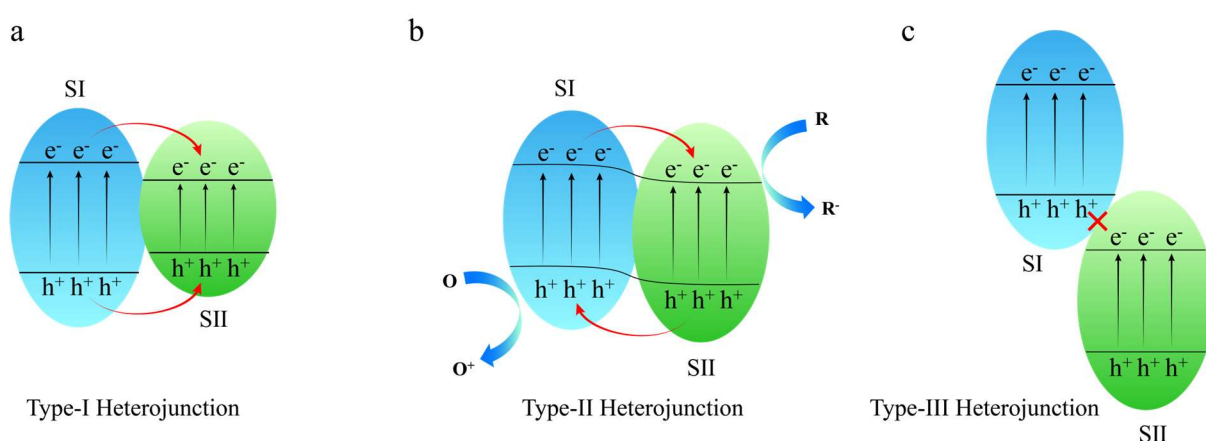
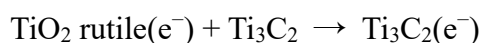
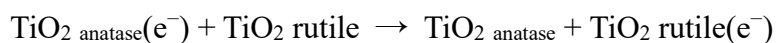
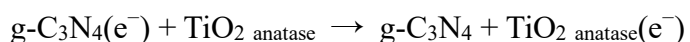
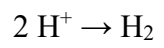
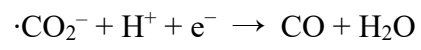
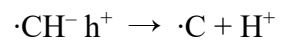
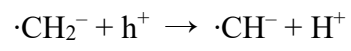
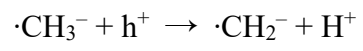
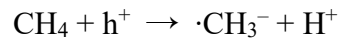


Figure 12. Schematic illustration of charge-carrier transfer in (a) type-I heterojunction with a straddling gap structure; (b) type-II heterojunction with a staggered gap structure; (c) type-III heterojunction with a broken gap structure.

4.1. Photocatalysts with type-II heterojunction structures.

For the PDRM reaction, Tahir et al. recently designed a 2D Ti₃C₂/TiO₂/g-C₃N₄ heterostructure photocatalyst (CN/TCT).[143] UV-vis spectra showed the absorption edges of TiO₂ and CN were 400 and 435 nm, respectively (**Figure 13a**). After coupling TC, CN/TCT formed an absorption edge at 440 nm. The energy band structure of individual semiconductors was determined by plotting the Tauc plot from the UV-Vis analysis, summarized in **Table 1**. PL spectra suggested a high separation efficiency of electron-hole pairs in CN/TCT, indicating that TC effectively mitigated the recombination phenomenon (**Figure 13b**). Therefore, the 2D CN/TCT composite achieved the maximum H₂ production rate of 30.2 μ·mol⁻¹ in 4 h, which was 2.8- and 5.4-fold of CN and TC, respectively (**Figure 13c and d**). According to the energy band structures, the type-II heterojunction pathway for the PDRM process was proposed (**Figure 13e**). Upon light excitation, the more negative potential of the excited electrons from CB of CN was quickly transferred to that of rutile TiO₂ through anatase TiO₂ that was ultimately captured by TC. TC as an electron receiver promoted the electron transfer from CN and TiO₂ to TC. The electrons accumulated on the surface of TC and then reacted with the adsorbed CO₂ molecules while the holes accumulated on the surface of CN and oxidized CH₄ molecules. The charge separation and PDRM reaction process of CO₂ and CH₄ were expected to proceed by the following steps:





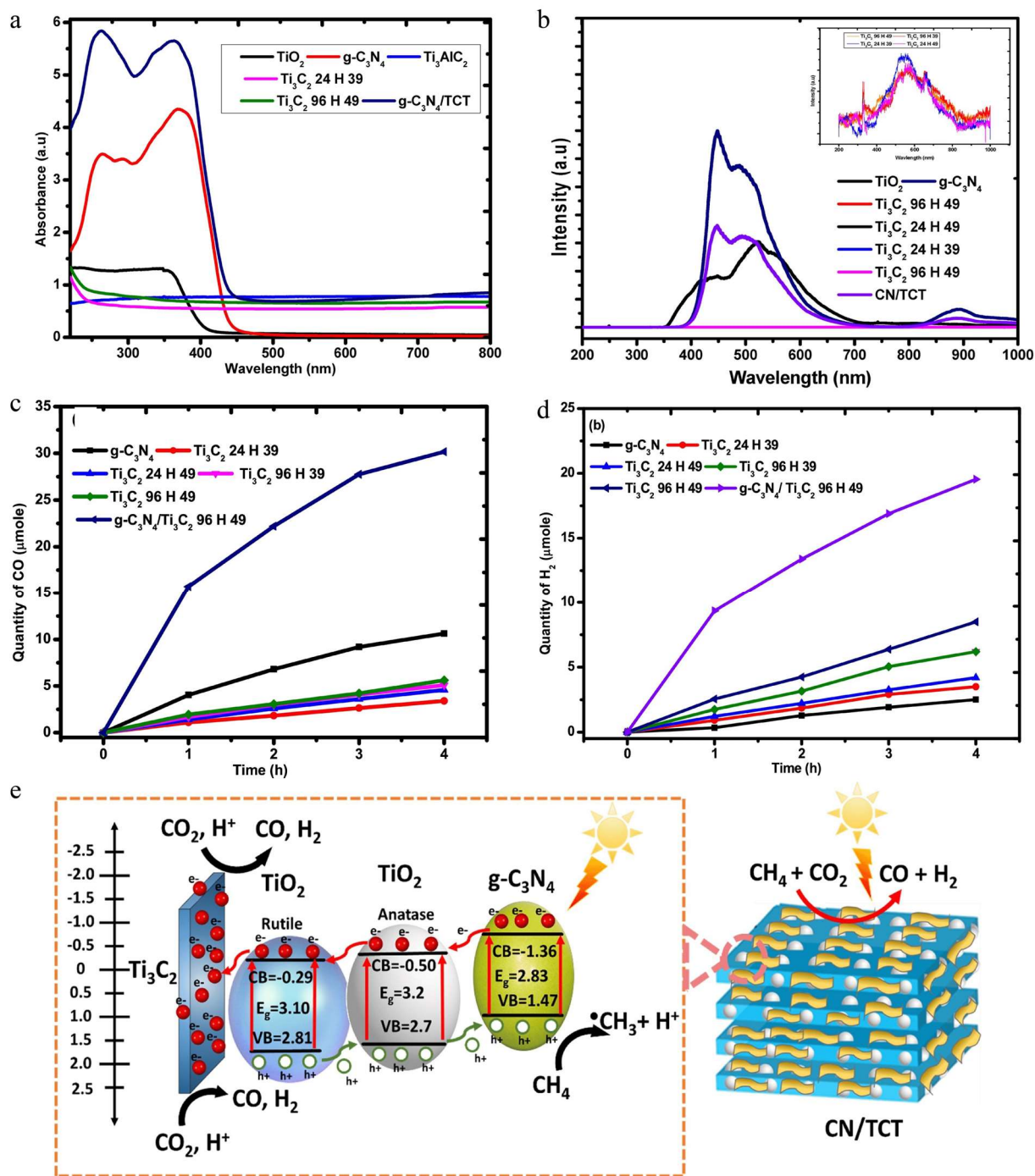


Figure 13. (a) UV-vis spectrum of TiO_2 , $\text{g-C}_3\text{N}_4$, Ti_3AlC_2 , Ti_3C_2 24 H 39, Ti_3C_2 96 H 49 and CN/TCT ; (b) PL spectra of TiO_2 , Ti_3C_2 24 H 39, Ti_3C_2 24 H 49, Ti_3C_2 96 H 39, Ti_3C_2 96 H 49 and CN/TCT . Photocatalytic production of (c) CO and (d) by Ti_3C_2 24 H 39, Ti_3C_2 24 H 49, Ti_3C_2 96 H 39, Ti_3C_2 96 H 49, and CN/TCT H_2 . (e) Schematic presentation of PDRM to CO and H_2 by CN/TCT photocatalyst.[143] Copyright 2021, Elsevier.

Table 1. Comparison of valance band, conduction band, and band gap (E_g) of TiO_2 , g- C_3N_4 , and CN/TCT composite catalyst.[143] Copyright 2021, Elsevier.

Sample	Band gap [eV]	Valance band [eV]	Conduction band [eV]
g- C_3N_4	2.83	1.47	-1.36
TiO_2 anatase	3.2	2.70	-0.50
TiO_2 rutile	3.1	2.81	-0.29
CN/TCT	2.86	1.57	-1.29

Although type-II heterojunction photocatalysts improve the electron-hole separation efficiency, the redox capacity of heterojunction composites is inevitably decreased, because reduction and oxidation reactions occur on the semiconductor with the lower reduction and oxidation potentials, separately. What's more, in type-II heterojunctions, the transmission of electrons and holes between two components is physically unfavorable due to the electrostatic repulsion. In this context, a Z-scheme mechanism for charge transfer has been proposed and used in the photocatalytic field as discussed below.

4.2. Photocatalysts with Z-scheme heterojunction.

Z-scheme photocatalyst was proposed by Bard et al. in 1979. Theoretically, a conventional Z-scheme photocatalytic system contains two semiconductors (SI and SII) and an acceptor/donor (A/D) pair (**Figure 14a**). During photocatalytic reactions, after the two semiconductors are excited by light to generate electron-hole pairs, the photogenerated holes of SI react with the electron donor D to generate the electron acceptor A, and the photogenerated electrons of SII react with the electron acceptor A to generate the electron donor D. The

electron-hole pairs in the two semiconductors are retained to participate in the redox reaction. Thus, through the conventional Z-scheme system, the spatial separation of redox sites can be realized, and the stronger redox reaction capability is maintained. However, there are some new problems owing to the additional redox electron mediators. Firstly, the charge transfer can only achieve sufficient efficiency in solution, limiting the system to solution-phase reactions. Secondly, due to the larger potential difference, the electrons in SI might react with A and the holes in SII react with D so that the charge transfer process is disturbed. Secondly, to ensure the redox electron pair can work properly, a certain pH condition must be satisfied. In order to overcome the above defects, an all-solid-state Z-scheme photocatalyst was proposed by Tada's group.[144]

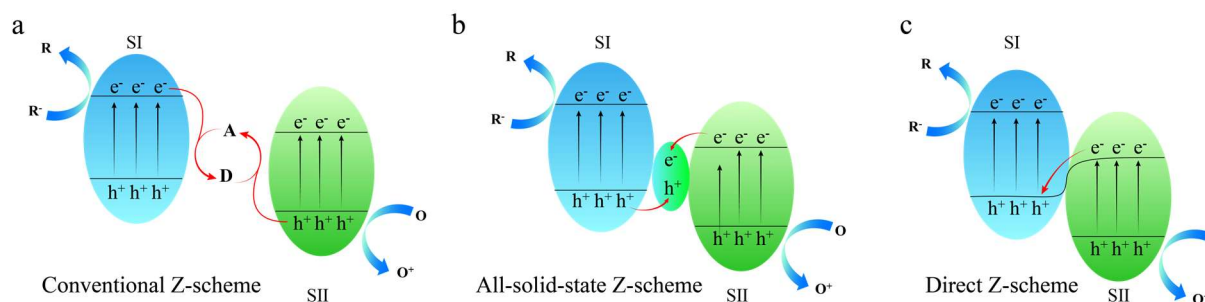


Figure 14. Schematic illustration of charge carrier transfer in (a) conventional Z-scheme photocatalysts; A and D stand for electron acceptor and donor, respectively; (b) all-solid-state Z-scheme photocatalysts; (c) direct Z-scheme photocatalysts.

All-solid-state Z-scheme photocatalysts consist of two different semiconductors and a solid electron mediator (**Figure 14b**). The photoelectrons from SII and holes from SI tend to transfer to an electron mediator and recombine. Consequently, the spatial electron-hole separation and optimization of the redox potential are achieved in solution, gas, and solid media. In an all-solid-state Z-scheme photocatalyst, the suitable electron conductor is important

because it determines the charge transfer efficiency and the stability of a photocatalytic system. Noble metals like Au, Ag, and Pt, are always proper candidates as electron mediators, while some conductive materials with excellent electronic conductivity (e.g. carbon-based materials) recently have been considered as potential substitutes for precious metals.[145–147] For instance, Liang et al. reported an all-solid TiO₂-TiC/g-C₃N₄ photocatalyst via a facile calcination method for PDRM.[148] The *in-situ* XPS spectra demonstrated the electronic states and charge transfer routes of the Z-scheme pathway (**Figure 15a–d**). The results showed that the light illumination increased the banding energy of both Ti 2p_{3/2} and Ti 2p_{1/2} by 0.4 eV, meaning a decline of electron density of Ti 2p, and thus electron flowing from TiO₂. The O 1s peaks at 530.1 eV and 532.3 eV from lattice oxygen and superficial hydroxyl groups were also increased, which was consistent with that of Ti 2P. For C 1s, the peak at 286.5 eV corresponding to the triazine structure of g-C₃N₄ was decreased after light exposure. Meanwhile, in N 1s XPS spectra, the peaks of N-(C)₃ and C-N-H shifted negatively under illumination, leading to the increasing electron density. Therefore, photoelectrons stayed at g-C₃N₄ instead of migrating to TiO₂, suggesting an all-solid Z-scheme charge transfer mechanism. The photoelectrochemical (PEC) experiments and PL spectra confirmed the effective electron-hole separation due to the Z-scheme heterojunction and excellent electronic conductivity of TiC (**Figure 15e**). In PDRM measurements, the photocatalytic performance of TiO₂-TiC/g-C₃N₄ was better than that of g-C₃N₄, TiO₂-TiC, and TiO₂/g-C₃N₄ (**Figure 15f**). The work functions and density of states (DOS) of TiO₂ and g-C₃N₄ were calculated, revealing that the work functions were 6.35 and 4.76 eV and bandgaps were 3.07 eV and 3.36 eV in TiO₂ and g-C₃N₄, respectively. The charge transfer in the all-solid Z-scheme heterojunction and the band structures were illustrated. According to

the CBs of g-C₃N₄ (−1.05 eV) and TiO₂ (−0.39 eV), it has been calculated that VBs were 2.02 eV for g-C₃N₄ and 2.97 eV for TiO₂, respectively. The difference in work function would cause the transfer of electrons from g-C₃N₄ to TiO₂ until the Fermi levels were aligned. Thus, the charge transfer led to more holes in g-C₃N₄ while more electrons in TiO₂, constructing an interfacial built-in electric field from g-C₃N₄ to TiO₂. Upon photoexcitation, photogenerated electrons would transfer from TiO₂ to g-C₃N₄ along the TiC mediator. The CB of g-C₃N₄ was negative enough for CO₂ photoreduction to CO (−0.53 eV), while CH₄ oxidation to H₂ occurred at the valence band of TiO₂.

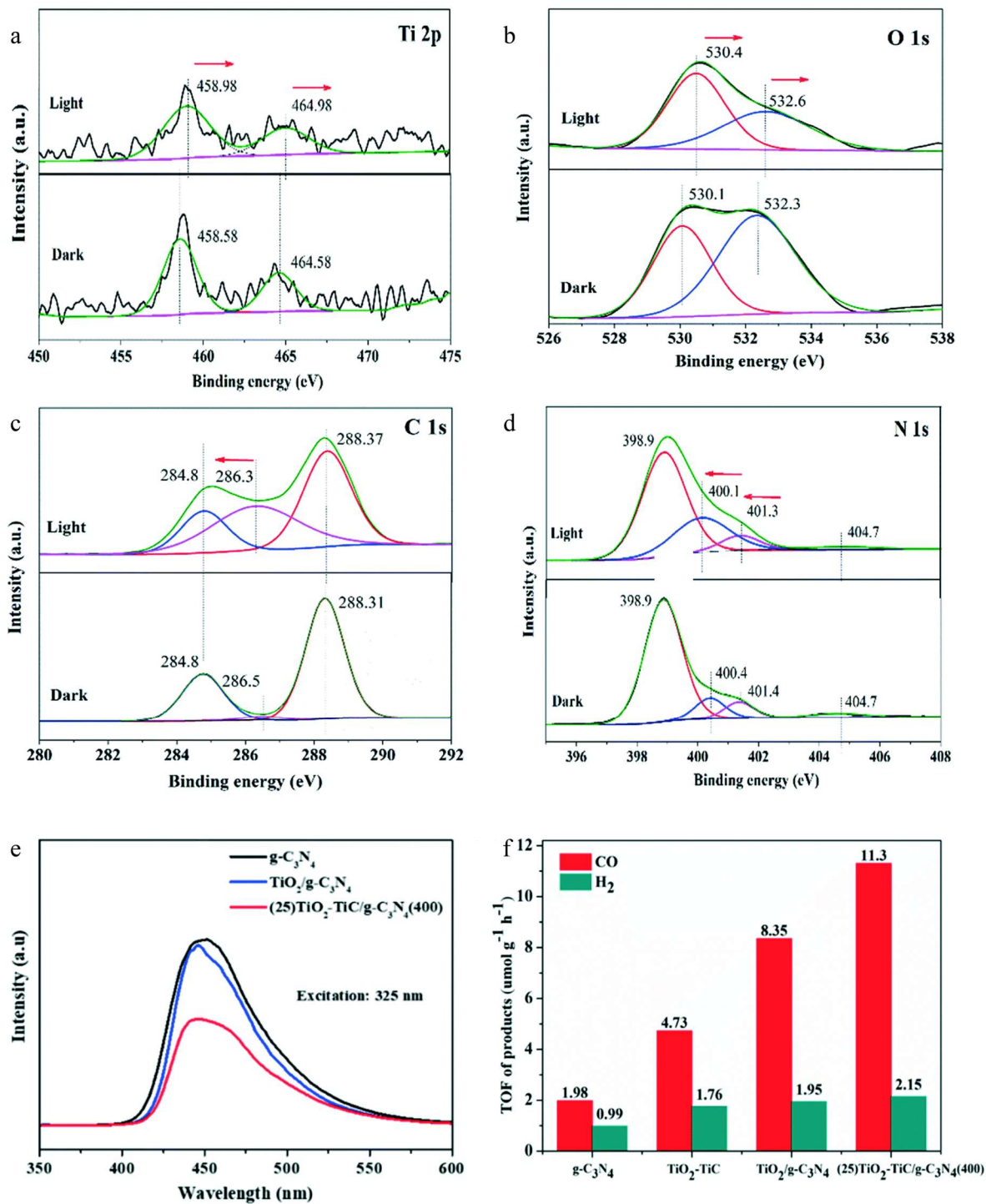


Figure 15. Ex-situ and *in-situ* high-resolution XPS spectra of (a) Ti 2p, (b) O 1s, (c) C 1s, and (d) N 1s regions. (e) photoluminescence (PL) emission spectra of $g-C_3N_4$, $TiO_2/g-C_3N_4$, and $(25)TiO_2-TiC/g-C_3N_4(400)$. (f) The performance for CO_2 photoreduction by $g-C_3N_4$, TiO_2-TiC , $TiO_2/g-C_3N_4$ and $(25)TiO_2-TiC/g-C_3N_4(400)$. Reaction conditions: P = 40 kPa; $CH_4:CO_2 =$

1 : 2; T = ambient room temperature.[148] Copyright 2022, Royal Society of Chemistry (RSC).

All-solid-state Z-scheme heterojunctions provide more opportunities for heterogeneous catalytic systems. However, most electron mediators required for improving the migration path for electrons in the all-solid-state Z-scheme photocatalysts are expensive and rare, which limits large-scale applications of these photocatalysts. In this circumstance, the concept of direct Z-scheme photocatalyst was first proposed by Xiao et al. in 2013.[149] Two semiconductors contact each other without an electron mediator so that the possible backward reactions from redox mediators and shielding effect from electron mediators could be suppressed significantly (**Figure 14c**). A typical charge transfer route in a direct Z-scheme system is staggered via the difference of work function between two semiconductors.[149] In detail, when SI and SII are in contact, free electrons in SI are able to migrate to SII, resulting in equilibrated Fermi levels. Hence, positive charges tend to accumulate on SI, and negative charges concentrate on SII, forming a built-in electric field and leading to band bending. Under light excitation, the electric field causes the recombination between photoelectrons from SII and photoholes from SI. With the assistance of the band bending phenomenon, the photoelectrons on the CB of SI will not transfer onto the CB of SII owing to the large potential barrier. Thus, the photoexcited electrons in SI and holes in SII can participate in reduction and oxidation reactions.

Direct Z-scheme photocatalysts are desirable for synthesizing fuels and high-value-added chemicals because of their preserved strong redox ability. For example, Mansoor and Tahir fabricated g-C₃N₄/CoAl-LDH/Ti₃AlC₂ with a direct Z-scheme heterojunction structure.[150] The ternary CoAl-LDH/g-C₃N₄/Ti₃AlC₂ composite reached the highest yield for CO and H₂ of 30.3 and 4.7 $\mu\text{mole}\cdot\text{g}^{-1}\cdot\text{h}^{-1}$ with selectivities of 86.5% and 13.5% during PDRM process

(**Figure 16a** and b). The improvement of CO and H₂ evolution rates could be attributed to the direct Z-scheme heterojunction structure, in which electrons transferred from g-C₃N₄ towards CoAl-LDH, and the excellent electronic conductivity of Ti₃AlC₂ made it a mediator by trapping electrons. Moreover, the photocatalytic biforming of methane (PBRM) experiments with an input feed mixture of CH₄, CO₂, and H₂O for syngas production (CO, H₂) were carried out (**Figure 16c** and d). The results showed adding H₂O to the feed mixture enhanced the oxidation and reduction processes, which determined the CO evolution rate. However, the productivity of CO from PBRM was 1.1 times lower than that from PDRM, attributed to the reactant competition between CO₂, CH₄, and H₂O. Thus, the high selectivity for CO in PDRM was due to RWGS, which resulted in lower H₂ and enhanced CO production.

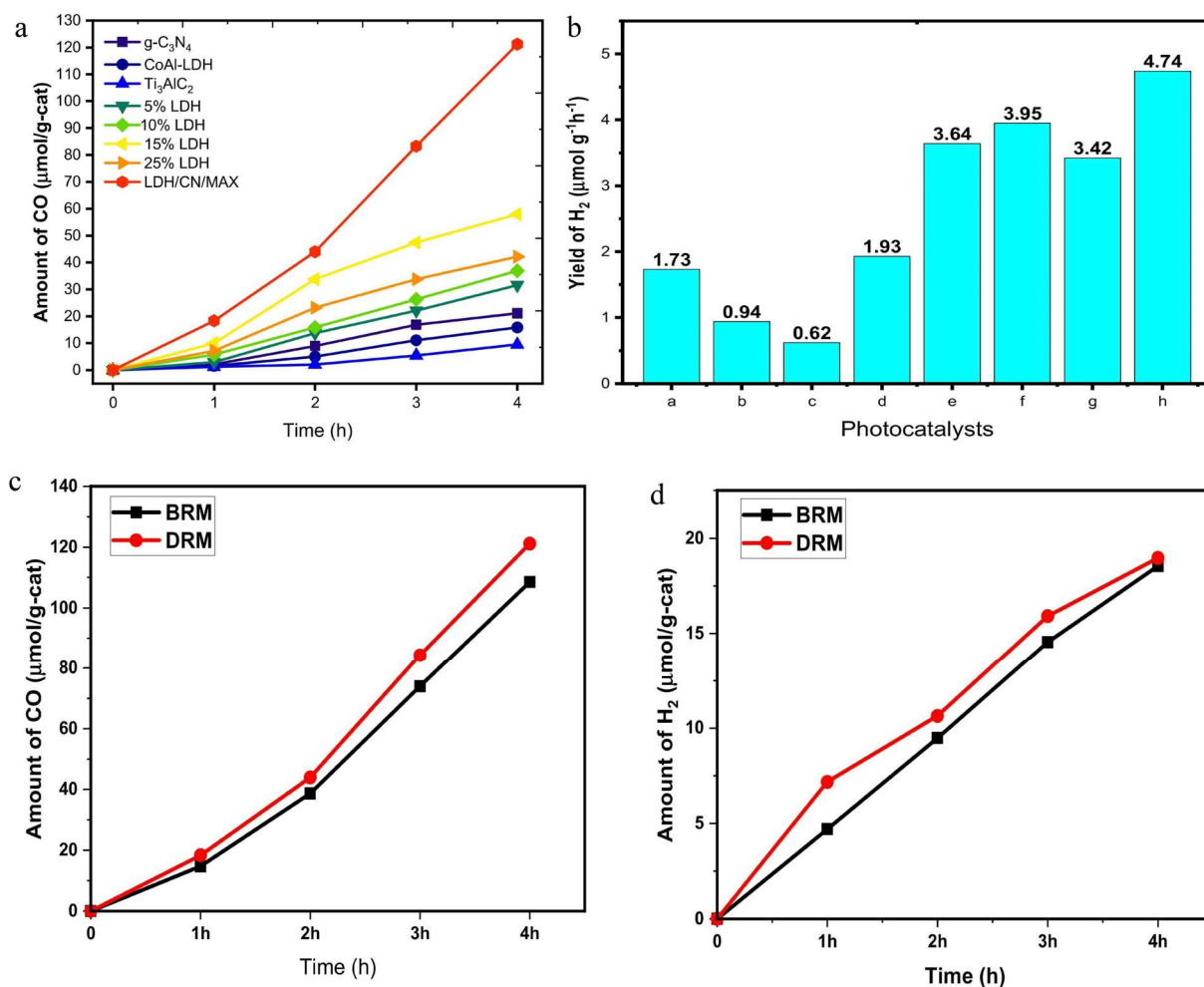


Figure 16. Comparative performance analysis of CoAl-LDH, $\text{g-C}_3\text{N}_4$, Ti_3AlC_2 , CoAl-LDH/ $\text{g-C}_3\text{N}_4$ and CoAl-LDH/ $\text{g-C}_3\text{N}_4/\text{Ti}_3\text{AlC}_2$ for syngas production using PDRM process: (a) CO production, (b) H_2 production; a = $\text{g-C}_3\text{N}_4$, b = CoAl-LDH, c = Ti_3AlC_2 , d = 5% CoAl-LDH/ $\text{g-C}_3\text{N}_4$, e = 10% CoAl-LDH/ $\text{g-C}_3\text{N}_4$, f = 15% CoAl-LDH/ $\text{g-C}_3\text{N}_4$, g = 25% CoAl-LDH/ $\text{g-C}_3\text{N}_4$, i = 15% CoAl-LDH-15% $\text{Ti}_3\text{AlC}_2/\text{g-C}_3\text{N}_4$. Performance comparison of CoAl-LDH/ $\text{g-C}_3\text{N}_4/\text{Ti}_3\text{AlC}_2$ composite in PDRM and PBRM process: (c) CO production, (d) H_2 production.[150] Copyright 2023, Elsevier.

Among various Z-scheme heterojunction photocatalysts, direct Z-scheme photocatalysts have obvious advantages compared to the traditional Z-scheme and all-solid-state Z-scheme photocatalysts. The superior photocatalytic performance of direct Z-scheme photocatalysts is

ascribed to the following four main aspects: (1) maintaining electrons and holes with strong redox capacity, (2) triggering reduction and oxidation reactions on different sites, (3) extending light absorption range, (4) utilizing advantages of both two semiconductors. Selecting semiconductors with appropriate energy bands determines the fabrication of direct Z-scheme photocatalysts. Only when the Fermi levels of two semiconductors can match each other, the direction of the built-in electric field induced by the redistribution of free charges is beneficial for charge transfer. Otherwise, the photocatalytic property will be decreased. In addition to the rational selection and design of semiconductors, the light response range and crystal structure are also crucial for achieving the specific photocatalytic redox reactions and accelerating the charge transfer at interfaces, respectively. For artificial photocatalysis technology, many fuels and high-value-added chemicals need photocatalysts with high redox potential. Due to the thermodynamic stability of reactants, high surface temperature over photocatalysts should be reached by light illumination during the photocatalytic process to rapidly complete the activation and dissociation of reactant molecules. Therefore, direct Z-scheme heterojunctions are one of the ideal candidates to realize the high photocatalytic activity and selectivity of products, solving the ever-growing environmental and energy crisis issues.

4.3. Photocatalysts with S-scheme heterojunction.

In the past few decades, science itself has evolved and changed, resulting in the increasingly sophisticated understanding and design of novel electron-hole separation/transfer mechanisms. Among innovative proposed charge transfer routes, Yu's group, who took the lead in nominating a Step-scheme (S-scheme) heterojunction based on the aforementioned Z-scheme heterojunction family, has shown the promising potential of S-scheme photocatalysts

for different photocatalytic applications.[151–153]

To understand the S-scheme charge transfer mechanism, it could sort photocatalysts into reduction and oxidation photocatalysts (RP and OP). RP possesses high CB, meaning that photoexcited electrons are effective, but the useless holes should be removed by sacrificial agents. On the contrary, in OP, the photoinduced holes are always utilized for photocatalytic oxidation reactions, while photoelectrons are fruitless. S-scheme photocatalysts are composed of RP and OP with staggered band structures similar to the energy band structure in type-II heterojunctions. However, the charge transfer route in S-scheme heterojunctions is totally different from that in type-II heterojunctions. RP has higher CB and VB positions and smaller work functions compared to OP. Thus, when the RP and OP are combined together in S-scheme photocatalysts, photoelectrons in RP could diffuse to OP spontaneously, forming the electron depletion layer and electron accumulation layer at the interface, respectively. In this case, negative-charged OP and positive-charged RP could lead to a built-in electric field, which accelerates the electron transfer from OP to RP. Besides, in consideration of their Fermi-level (work function), the shift of Fermi-level lead to the energy band bending, resulting in the recombination between photoholes from OP and photoelectrons from RP. Meanwhile, the Coulombic attraction can also promote the recombination between the photogenerated electrons over CB of OP and holes over VB of RP at the interface. Therefore, an S-scheme heterojunction is able to maintain the strong redox capacity of OP and RP via the interface electric field and interaction between the energy band in RP and OP.

PDRM needs a complete redox reaction for reducing CO_2 and oxidizing CH_4 , corresponding to the advantages of S-scheme photocatalysts. Unfortunately, in the PDRM area,

almost no study focuses on the relationship between PDRM efficiency and S-scheme photocatalysts. Tahir's group tried to fabricate $\text{TiO}_2/\text{g-C}_3\text{N}_4$ -based S-scheme heterojunctions and display the improvement of PDRM activity over $\text{TiO}_2/\text{g-C}_3\text{N}_4$ -based S-scheme photocatalysts to some extent,[79,154] but their works mainly accumulated on the CO_2 photoreduction application and the comparison between different reductants (e.g. CH_4 , H_2 , H_2O) for CO_2 reduction instead of the in-depth investigation of the interaction between CH_4 and CO_2 or the relative enhancement mechanism from S-scheme charge transfer pathway during PDRM reactions. Thus, this topic should obtain enough attention in future studies, because the above-mentioned advantages of S-scheme heterojunctions have displayed positive influences in the PDRM field. The design of S-scheme heterojunctions for PDRM application should refer to other systematic works in other CH_4 conversion technologies and CO_2 photoreduction field since most of them fully utilize the advantages of S-scheme heterojunctions (strong redox ability and enhanced charge transfer kinetics) to complete both reduction and oxidation processes without sacrificial agent and enhance the catalytic performance. For example, ZnO , BiVO_4 , WO_3 , and TiO_2 as easily accessible semiconductors have been widely utilized in constructing S-scheme photocatalysts owing to their low VB (~ 2.43 eV for ZnO , 1.99 eV for BiVO_4 , 2.8 eV for WO_3 and 2.81 eV for TiO_2).[155–157] And $\text{g-C}_3\text{N}_4$ and BiOBr had strong reduction ability due to their high CB (~ -0.68 eV for $\text{g-C}_3\text{N}_4$ and -0.70 eV for BiOBr) so that they are often used as reduction sites in S-scheme heterojunctions.[158,159] Thus, it could be expected that a reasonable combination between the above semiconductors could improve the PDRM catalytic activity. What's more, in recent years, some works tried to use covalent organic framework (COF) or metal organic framework (MOF) materials to fabricate S-scheme

photocatalysts because of the well-designed pore structure, wide light absorption performance, reactants (e.g. CO₂) capture capability, and π -electrons delocalization effect.[160–162] Therefore, the COF/MOF materials and their derivatives might also contribute to the development of S-scheme heterojunction photocatalysts for PDRM reaction.

5. Photocatalysts with LSPR effect

When the dimension of metal NPs is smaller than the wavelength of the incident light, the free electrons in plasmonic metal NPs will induce a coherent collective oscillation due to the response to an external oscillating electric field. The asymmetrical distribution of electron cloud in plasmonic metal NPs causes a Coulombic restoring force between negative electrons and positive nuclei. Thus, a built-in electric field with the opposite direction to the external field is constructed owing to a series of oscillations of electrons (similar to a stretched spring) and redistribution of charge density.[163,164] The oscillation and electric field are regarded as the LSPR effect. For photocatalysis, the enhancement effects from LSPR mainly include extending light absorption range, hot-electron injection, and plasmon-induced resonance energy transfer (PIRET, **Figure 17**).[164]

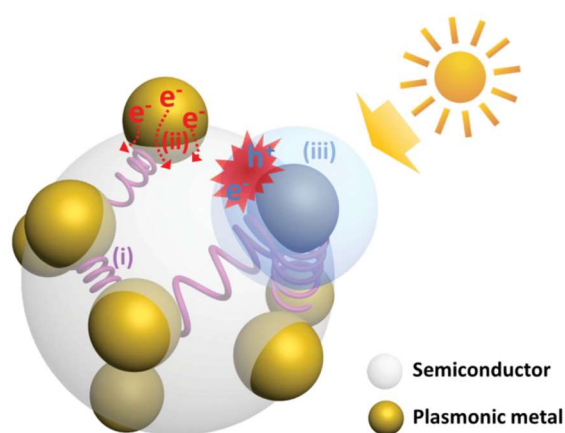


Figure 17. Schematic illustration of the three mechanisms for the enhancement effect of

plasmonic materials: i) light absorption and scattering; ii) hot-electron injection and iii) PIRET.[164] Copyright 2015, Wiley.

In this section, we focus on the influence of PIRET on photocatalytic performance because it can adjust charge transfer dynamics. PIRET first proposed by Wu et al. in 2012 is the non-radiative transfer of energy from plasmonic metals to semiconductor photocatalysts.[165] Although bulk semiconductors can generate a lot of electrons and holes, the charge tends to recombination before transferring to the surface. The PIRET maintains the number of photoexcited charges while reducing the thickness of semiconductors, ensuring enough charge could participate in photocatalytic reactions over the surface of photocatalysts.[166] Optical simulations (e.g., finite-difference time-domain and finite element method) have demonstrated that the PIRET process promotes charge-carrier separation with the assistance of the local electromagnetic field. Notably, only when the photonic energy is above the optical bandgap of the semiconductor, the enhanced separation and transfer can be achieved. Moreover, since the formation rate of the charge-carrier in the semiconductor is proportional to the square of the local intensity of the electric field ($|E|^2$), the strong LSPR-induced electromagnetic field (PIRET) increases the generation of electron-hole pairs.[167,168]

One of the focuses of PIRET is how to design reasonable experiments to test and understand the enhancement mechanism. Initially, the contribution of the LSPR effect in enhanced transfer dynamics was confirmed by comparing the PEC performance of photoanodes with metal NPs (**Figure 18a–d**).[169] Recently, Cronin's group and Zhang's group utilized finite-difference time-domain (FDTD) simulation and density functional theory (DFT) calculation to prove that the local electromagnetic field from PIRET could effectively shorten

the distance of charge transfer.[170,171] Besides, Linic et al. confirmed that the interaction between localized electric fields and surrounding semiconductors allowed the formation of electron-hole pairs (**Figure 18e–g**). This kind of charge-carrier near the semiconductor surface was easy to transfer to the surface, taking part in subsequent redox reactions.[172]

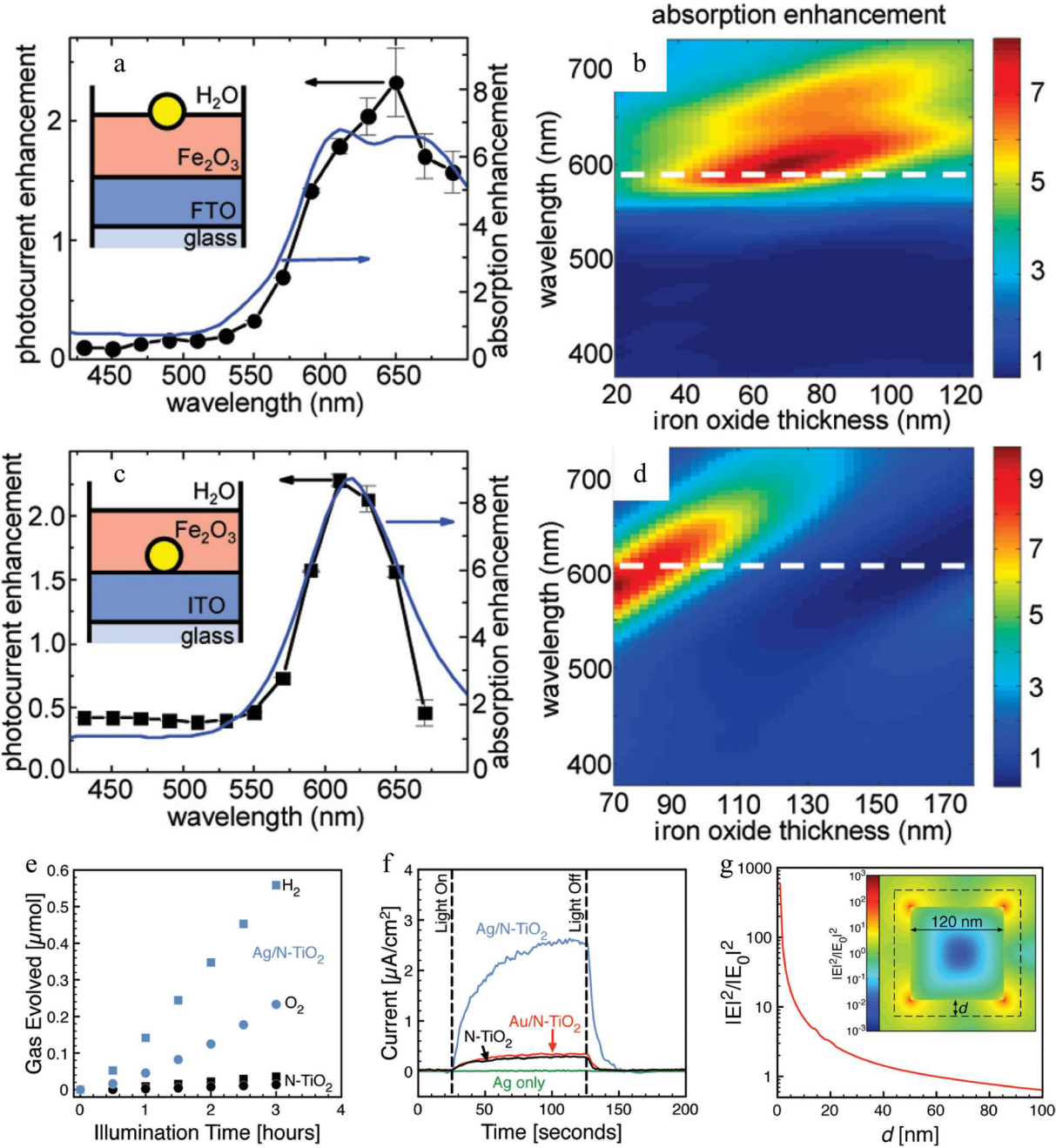


Figure 18. (a, c) Measured photocurrent enhancement spectra (black symbols) and electromagnetic simulations (blue lines). (b, d) Full-field electromagnetic simulations of the

plasmon-enhanced absorption in a probe region near the Au particle and at the $\text{H}_2\text{O}/\text{Fe}_2\text{O}_3$ interface predict strong enhancements near the surface plasmon resonance. The dashed white lines indicate the surface plasmon resonance wavelength for a 50 nm Au nanoparticle located on top of or embedded in a semi-infinite Fe_2O_3 , respectively.[169] Copyright 2011, American Chemical Society (ACS). (e) H_2 and O_2 production upon visible illumination of N-TiO₂ (black symbols) and Ag/N-TiO₂ (blue symbols) photocatalysts, as measured by mass spectrometry. (f) Photocurrent responses (per macroscopic electrode area) upon illumination with a broadband visible light source (400-900 nm). (g) Average electric field enhancement around an Ag cube with an edge length of 120 nm as a function of the distance d from the cube, as calculated using FDTD simulations. Inset: Local enhancement of the electric field calculated from an FDTD simulation of a 120 nm Ag cube in water.[172] Copyright 2011, American Chemical Society (ACS).

Research on the relationship between LSPR and PDRM efficiency has also been carried out.[173] Liu et al. first reported plasmonic Au through the LSPR effect to facilitate the polarization and activation of CO_2 and CH_4 .[174] The highly energetic electrons from Au enhanced the catalytic performance of Rh/SBA-15 by 1.7 times in DRM reaction under visible light excitation. Cu as non-noble metal was also reported that its LSPR effect could accelerate the activation process of CH_4 and CO_2 at room temperature. The light-excited hot carriers significantly reduced the barrier for the dissociation of reactants without external thermal energy input so that the large energy consumption and deactivation of catalysts could be avoided by plasma-assisted photocatalysis.[174] For the enhancement effect of LSPR via strong local electric fields (PIRET) in PDRM activity, Liu et al. used CO_2 as an oxidant for reforming CH_4

into CO and C₂H₄ over TiO₂-supported Ag nanoparticles.[175] The highest evolution rates of CO and C₂H₄ achieved 2298 μmol·g⁻¹ and 1372 μmol·g⁻¹ over Ag/TiO₂ under solar irradiation (**Figure 19a**). However, when the photocatalyst was illuminated by UV light, one of the main products, C₂H₄, would be replaced by C₂H₆ (**Figure 19b**). The XPS spectra of Ag were obtained to demonstrate the role of Ag (**Figure 19c–f**). The results showed the zero metallic state of silver, corresponding to the binding energies of 374.1 and 368.1 eV for Ag 3d, before the reaction. But when the composite photocatalyst was exposed to visible light, the transformation of the state from Ag(0) to Ag(I) was observed, indicating strong plasmon resonance. The authors believed that the visible light would excite the LSPR effect in Ag NPs, enabling more hot electrons to migrate into TiO₂ instead of staying at the surface of Ag. Due to the directional transfer of charges, the electrons overcoming the Schottky barrier and injecting into TiO₂ caused the CO₂ reduction and CH₄ oxidation on different sites, separately. Besides the coupling LSPR and photoelectric effect, simultaneously LSPR effect from two plasmonic metals to promote DRM was also studied recently. Ye's group investigated the influence of plasmonic coupling effect of Pt and Au NPs in DRM reaction.[176] The photocatalytic performance of Pt-Au/SiO₂ and Pt/SiO₂ were 68.6 and 46.6 μmol·g⁻¹·min⁻¹, respectively, which were about 2.4 and 1.6 times higher than those of the thermal catalytic process, separately. FDTD method was conducted to understand the influence of LSPR (**Figure 19g–l**). The electric field distributions under UV and visible light excitation were simulated. It could be observed that the intensity of built-in electric field over Au and Pt NPs was increased by 530 nm light irradiation. What's more, the coexisting of Au and Pt over SiO₂ furtherly enhanced the electric field. Thus, the strong near-field coupling was beneficial for the participation of electrons into dissociation of C–H or C=O bonds and

reduction reactions. Thus, LSPR effect with PIRET is a promising strategy to accelerate the photocatalytic synthesis of various fuels via strong localized electromagnetic field enhancing charge transfer dynamics.

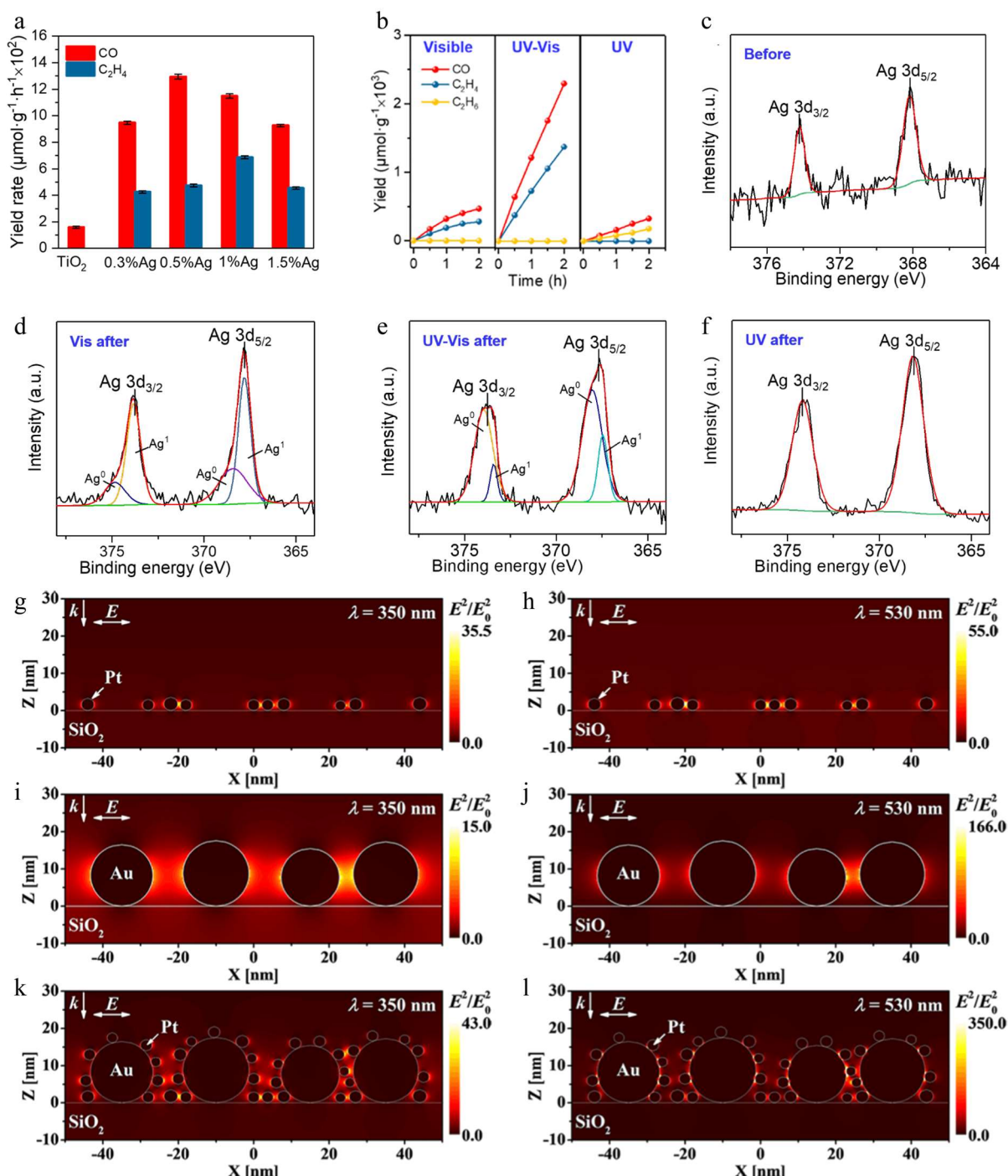


Figure 19. (a) The specific activities over different amounts of Ag-containing composites under simulated solar irradiation. (b) Photocatalytic performance for CO_2 and CH_4 reformation: the

effect of different light sources (visible light, simulated sunlight, and ultraviolet light) over 1%Ag/TiO₂ catalyst. High-resolution XPS spectra of Ag (c) before, (d) after reaction under visible light irradiation, (e) after reaction under simulated solar irradiation, and (f) after ultraviolet light irradiation.[175] Copyright 2019, American Chemical Society (ACS). Spatial distribution of the enhancement of electric field intensity at wavelengths of 350 and 530 nm, from FDTD simulation of (g, h) Pt/SiO₂, (i, j) Au/SiO₂, and (k, l) Pt-Au/SiO₂. [176] Copyright 2018, American Chemical Society (ACS).

In recent years, the LSPR mechanism was gradually improved in various photocatalytic systems and applications.[172,177] Many well-designed experiments were conducted to provide more insights into LSPR. Although the LSPR effect with PIET has been widely recognized to adjust the charge transfer behavior, this theory did not attract enough attention in PDRM research yet. Moreover, the structural optimization between plasmonic metals and semiconductors and the hard requirements for light conditions are still challenges.[164] These problems are urgent to be solved.

6. *In-situ* characterization and theoretical calculation

With the development of the PDRM technology, more requirements have been proposed to understand the reaction mechanism or clarify the effects of specific components in photocatalysts. Therefore, great attention has been paid to the *in-situ* characterization techniques and theoretical calculation. Under the model or true reaction conditions, these advanced methods not only verify some controversial hypotheses like reaction pathways and charge-carrier transfer routes but also may observe new phenomena and even summarize novel theories.[178–180] In this section, the main roles and benefits of *in-situ* experiments and

theoretical calculations will be summarized to provide references for future studies.

1) Monitoring crystallinity or phase evolution during the synthesis process. Many works have reported the relationship between catalytic properties (e.g. activity and stability) and crystal structures via *in-situ* XRD, XAS, and XPS.[181–184] And these characterizations provide rational explanations for the high efficiency and stability of catalysts under harsh DRM conditions. For instance, Coster's group investigated the evolution of the constituents of an 8 wt%Ni-5 wt%Fe/MgAl₂O₄ catalyst for DRM by *in-situ* quick X-ray absorption spectroscopy (QXAS).[182] During the preparation process, the element states of Fe were NiFe₂O₄ at the surface and MgFe_{3+x}Al_{2-x}O₄ within the support (**Figure 20a**). On the contrary, Ni was presented as NiO (**Figure 20b**). During the reduction process, NiFe₂O₄ and NiO form a Ni-Fe alloy. And MgFe_{3+x}Al_{2-x}O₄ was partially reduced to MgFe_{2+x}Al_{2-x}O₄. Thus, Ni-Fe alloy, MgFe_{2+x}Al_{2-x}O₄, and MgFe_{3+x}Al_{2-x}O₄ were the main phases after reduction treatment. In DRM experiments, the excessive CO₂ atmosphere (CH₄ : CO₂ = 1 : 2 or 1 : 1.5) led to the formation of FeO_x on the Ni-Fe surface, affecting the DRM activity and even causing some reincorporation of Fe into the support (**Figure 20c** and **d**). For prevalent reaction condition (CH₄ : CO₂ = 1 : 1), the CH₄ dissociation process counteract the oxidation from CO₂ so that no obvious change was monitored in catalyst (**Figure 20e**).

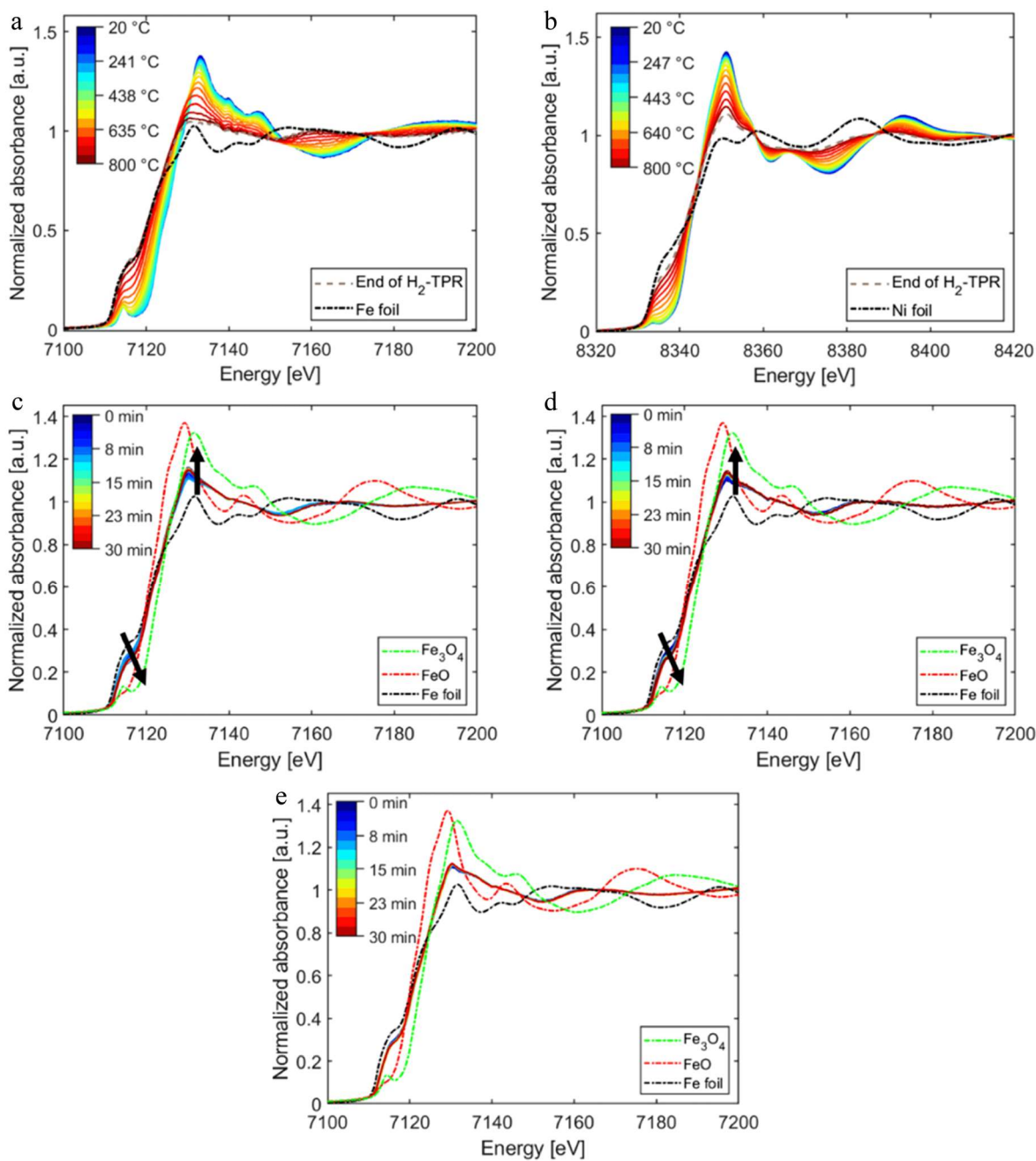


Figure 20 *In-situ* QXANES spectra recorded during H₂-TPR (10 °C/min, up to 800 °C, for 30 min) of as-prepared 8Ni5Fe/MgAl₂O₄ at (a) the Fe K edge and (b) the Ni K edge. *In-situ* Fe K edge QXANES spectra recorded during DRM (750 °C, 1 atm, 30 min) of reduced 8Ni5Fe/MgAl₂O₄ with CH₄/CO₂ = (c) 1/2, (d) 1/1.5 and (e) 1/1. Solid lines: experimental spectra; dashed lines: reference spectra; bold arrows: evolution of the spectra during DRM.[182]

2) Observing the charge transport and active center variation. *In-situ* XPS and XAS experiments can directly observe charge transport or the active components variation by recording and comparing the elemental status in photocatalysts under light irradiation. A practical example is a Si/ZrO₂ catalyst with the high initial conversion efficiency of both CH₄ (0.50 s⁻¹) and CO₂ (0.44 s⁻¹) and stability for DRM reaction at a low-temperature (400 °C).[185] And the authors investigated the states of Ni, Si, and Zr elements under reaction conditions via *in-situ* XPS spectra. The XPS results of Ni 2p indicated most NiO were converted into Ni⁰ species, on which the dissociation of C–H bonds as the limiting step for DRM reaction tend to occur (**Figure 21a**). After the DRM reaction at 400 °C, the intensity of Ni had a decline over the Ni-Si/ZrO₂ catalyst because of the carbon coating on Ni. But most Ni⁰ species could still be observed on Ni-Si/ZrO₂ catalyst within 20 min and even 60 min reaction, meaning the existence and stability of Ni⁰ due to the interaction between Ni and support. However, on Ni-Zr/SiO₂, the peak of Ni 2p shifted to higher binding energy under the reaction conditions (**Figure 21b**). After 60 min reaction, the Ni⁰ species almost faded away, suggesting the formation of NiO. Thus, the activity of Ni-Zr/SiO₂ catalyst gradually decreased within 5 h. In addition to the variation of the Ni binding energy, it should also be noted that the position of peaks of P1 (~ 854.5 eV for Ni²⁺) and P2 (~ 857.0 eV for Ni²⁺) in Ni-Zr/SiO₂ had a shift to higher binding energy under reaction conditions, proving that the ability of nickel species to donate electrons to ZrO₂ modified by silica was stronger than that to SiO₂ modified by ZrO₂. And the XPS spectra of Zr 3d over Ni-Si/ZrO₂ showed that the peaks at 182.6 eV corresponding to ZrO₂ shifted to lower binding energy, meaning the accumulation of charges on the ZrO₂ surface (**Figure 21c**). On the contrary, the peak of Zr 3d in Ni-Zr/SiO₂ had higher binding

energy, meaning charges tend to transfer from Zr surface to ZrO₂ (**Figure 21d**). For O 1s XPS spectra, the peak at ~ 528 eV was attributed to the oxygen ions (O²⁻), which was beneficial for the activation of C–H bonds (**Figure 21e and f**). Therefore, the higher content of O²⁻ in Ni-Si/ZrO₂ than that in Ni-Zr/SiO₂ improved the DRM activity of Ni-Si/ZrO₂ catalyst. Indeed, this work provided timely details for different element changes in catalysts during the reaction process, confirming that *in-situ* XPS is an effective strategy to in-depth study the influences of element states in catalytic performance. Besides the surface states, the charge transfer behavior in some photocatalysts (especially in S-scheme photocatalysts) with the built-in electric field was gradually reported by the above *in-situ* characterizations,[186–189] we hope this advanced technology could be utilized for electric field-assisted PDRM field for proving some uncertain ideas or providing novel theories.

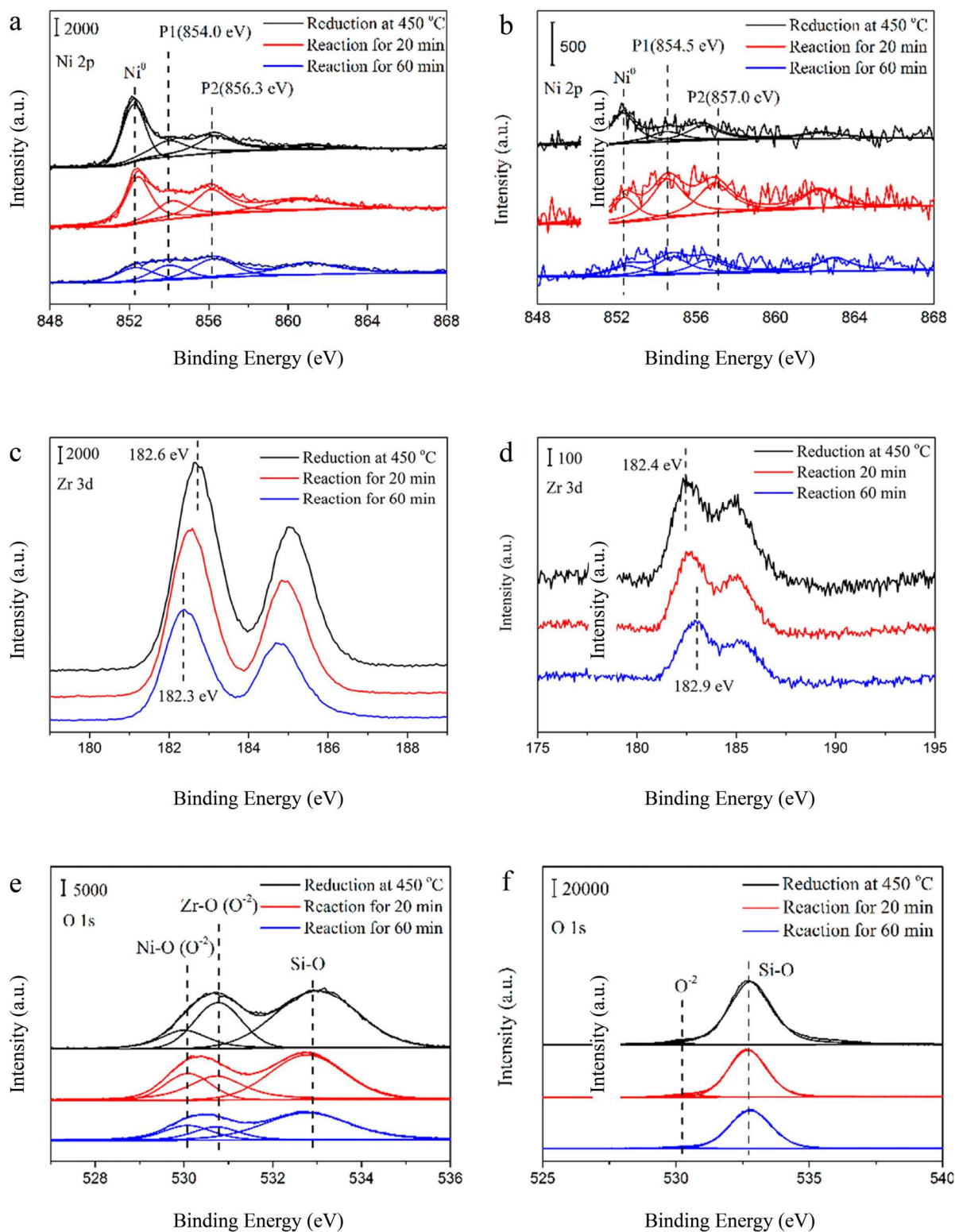


Figure 21 *In-situ* XPS spectra of Ni-Si/ZrO₂ and Ni-Zr/SiO₂ catalysts after reduction at 450 °C with a mixed flow ($F(\text{H}_2) = F(\text{Ar}) = 30 \text{ mL min}^{-1}$) and reaction at 400 °C with a mixed flow ($F(\text{CH}_4) = F(\text{CO}_2) = 30 \text{ mL min}^{-1}$): (a) Ni 2p, (c) Zr 3d, and (e) O 1s for Ni-Si/ZrO₂ catalyst

and (b) Ni 2p, (d) Zr 3d, and (f) O 1s for Ni-Zr/SiO₂ catalyst.[185] Copyright 2018, American Chemical Society.

In addition, Senanayake's group prepared a Co-loaded CeO₂ catalyst and studied the interaction between CO and CeO₂ during DRM reactions via the *in-situ* time-resolved X-ray diffraction (TR-XRD) method.[190] The results of TP-XRD showed when the temperatures were 200–350 °C, an interaction between CH₄ and CoO_x-CeO₂ could be observed (**Figure 22a**). The H₂ from C–H dissociation caused the reduction of Co₃O₄ and even a part of CeO₂, forming Co and Ce³⁺. During the DRM process, according to the decline of CH₄ peak intensity, the decomposition of CH₄ was carried out on Co metals at ~ 520 °C (**Figure 22b**). The production of CO and H₂O suggested that the oxygen atoms from CeO₂ took part in the CH₄ oxidation and inhibit the activation from possible carbon deposition. Through TR-XRD, the charge interaction between reactants and active components was demonstrated. Anchoring Co onto the CeO₂ surface could avoid the coke formation and form a closed catalytic cycle (CeO₂ + CH₄ → CeO_{2-x} + C + H₂/H₂O; Co₃O₄ → Co–O + C → Co + CO) at the interface via the synergistic effect between Co and CeO₂.

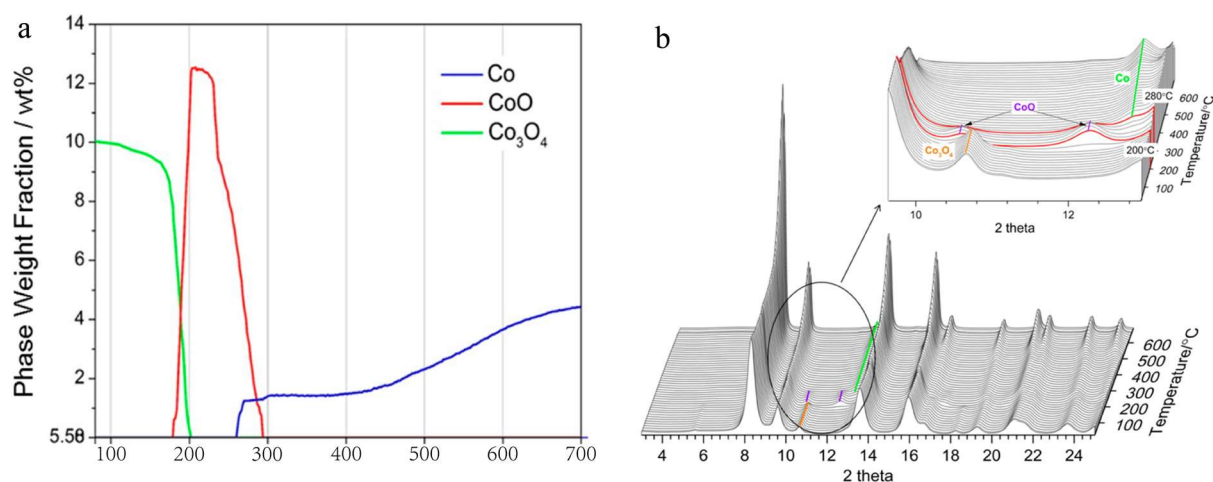


Figure 22 (a) Cobalt-containing phases as weight fractions as a function of temperature during

the H₂-TPR on a 10 wt % Co–CeO₂ catalyst. (b) Sequential in situ XRD patterns acquired while performing the H₂-TPR on a 10 wt % Co–CeO₂ catalyst.[190] Copyright 2018, American Chemical Society.

3) Studying the photocatalytic reaction mechanism. More specific reaction mechanisms might be observed by analyzing intermediates (e.g. radicals and molecules) and products using *in-situ* electron paramagnetic resonance (EPR) and diffuse reflectance infrared Fourier transform spectroscopy (DRIFT) spectra.[191–193] Currently, the *in-situ* DRIFT spectra have been widely utilized for artificial fuel synthesis via photocatalysis. In the PDRM field, a suitable example was reported by Li's group.[194] In this work, a Pt catalyst supported on an equimolar Al₂O₃–CeO₂ binary oxide (Pt–Al–Ce) was applied in a photothermal DRM reaction. Compared with Pt/CeO₂ (Pt–Ce) and Pt/Al₂O₃ (Pt–Al) catalysts, Pt–Al–Ce catalyst exhibited an H₂ and CO production rate of 657 and 666 mmol·g⁻¹·h⁻¹ with the H₂/CO ratio almost equal to unity, respectively. What's more, the apparent activation energy (E_a) for H₂ and CO production under dark conditions was 62.3 kJ mol⁻¹ and 41.9 kJ mol⁻¹, respectively. However, the apparent E_a under irradiation was only 39.8 kJ mol⁻¹ and 27.8 kJ mol⁻¹. Experimentally, the yield rate of syngas under light irradiation was much higher than that under dark-thermal conditions, meaning that light illumination could reduce the reaction activation energy. To investigate the solar light effect and possible intermediates from the photocatalytic reduction and oxidation process, *in-situ* DRIFTS spectra were obtained on Pt–Al–Ce and Pt–Ce under dark and light conditions. When CH₄ and CO were absorbed by Pt–Al–Ce and Pt–Ce, the formation of formate (HCOO⁻), bidentate carbonate (b-CO₃²⁻), and monodentate carbonate (m-CO₃²⁻) could be observed as marked on *in-situ* DRIFT curves (**Figure 23a** and c). The intensities of the

carbonate absorption bands ($1600\text{--}1200\text{ cm}^{-1}$) were lower on Pt–Al–Ce than Pt–Ce due to the lower concentration of CeO₂ in the Pt–Al–Ce. And the signal intensity of the Pt–CO absorption band on Pt–Al–Ce was stronger than that on Pt–Ce. Under light condition, the peaks of HCOO[−] and b-CO₃^{2−} intermediates were weaker, suggesting a promoted reaction rate in the DRM process (**Figure 23b** and d). Therefore, the above work confirmed that *in-situ* characterizations can not only determine the accurate reaction routes by detecting the intermediates but also display the advantages of light illumination, which induced charge-carrier and promote activation, in PDRM efficiency.

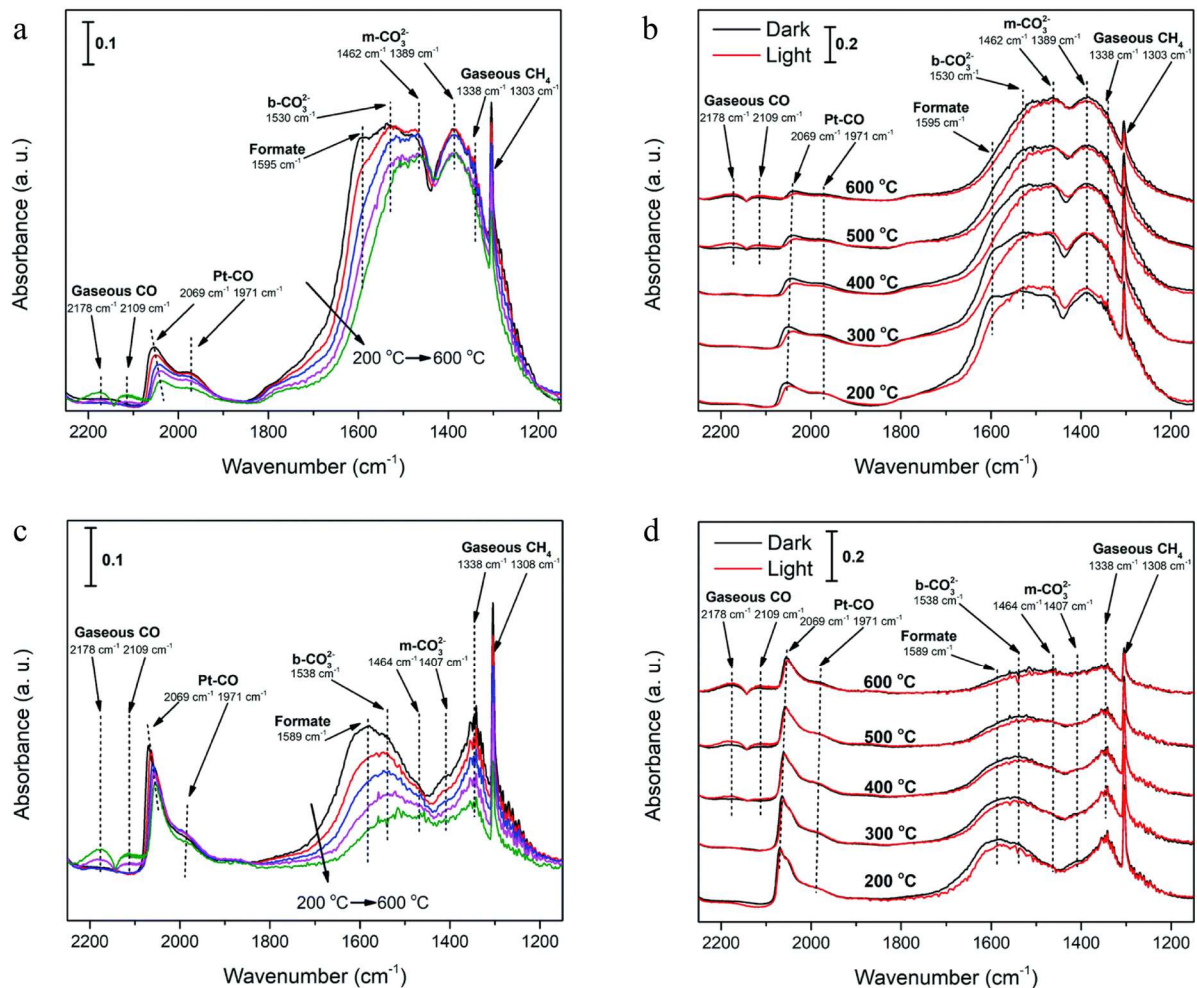


Figure 23 *In-situ* DRIFTS spectra under DRM reaction conditions in the dark on (a) Pt–Ce and (c) Pt–Al–Ce and dark–light comparison on (b) Pt–Ce and (d) Pt–Al–Ce.[194] Copyright 2022

Royal Society of Chemistry.

The possible reaction routes can be also predicted by DFT calculation via estimating the energy barrier of each step during the DRM reaction. And DFT method can also study the energy band structure, electronic structure, as well as molecular orbitals for explaining the photocatalytic ability.[195] For instance, Li et al. designed a novel metal-free porous covalent organic polymer (TPE-COP) for efficient PDRM application.[196] The push-pull effect between the electron donor (tris(4-aminophenyl)amine, TAPA) and acceptor (4,4',4'',4'''-((1 E,1' E,1'' E, 1'''E)-(ethene-1,1,2,2-tetrayltetrakis (benzene-4,1-diyl))tetrakis (ethene-2,1-diyl))tetrakis (1-(4-formylbenzyl)quinolin-1-ium), TPE-CHO) in TPE-COP promoted the separation of photogenerated electron-hole, thus greatly improving the photocatalytic activity. And the PDRM experiments showed the evolution rates with 1123.6 and 30.8 $\mu\text{mol}\cdot\text{g}^{-1}$ for CO and H₂, respectively, higher than those of TPE-CHO molecules. To further explain their results, DFT calculations were carried out for displaying the electronic structure and corresponding leading molecular orbitals (**Figure 24a**). The unit structure of TPE-COP showed the highest occupied molecular orbital (HOMO) was mainly in TAPA, while the lowest unoccupied molecular orbital (LUMO) was in TPE-CHO, meaning that there should be a donor-acceptor pair in this composite catalyst. Meanwhile, the HOMO-LUMO energy gap of TPE-COP was 1.148 eV, lower than that of TPE-CHO (4.761 eV), corresponding to a red shift in UV-vis spectra and benefiting photocatalytic capacity (**Figure 24b**).

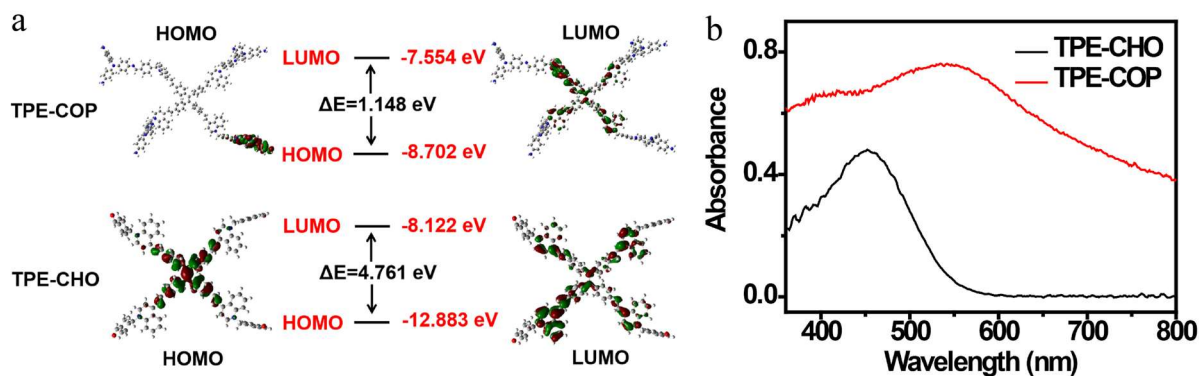


Figure 24 (a) DFT calculation for TPE-COP and TPE-CHO: HOMO–LUMO transitions. (b) The UV-vis spectra of TPE-CHO and TPE-COP.[196] Copyright 2023, Elsevier.

In addition to the above benefits and related practical instances, some potential effects of *in-situ* characterization and theory calculation/simulation are also introduced below. Some of them have been realized in other photocatalytic fields.[178]

1) Studying the roles of defects. Defects can be induced by light irradiation or reaction with water, oxygen, carbon dioxide, and many other ubiquitous molecules.[197] By *in-situ* XPS, XAS, FTIR, and Raman spectroscopy, new chemical compositions on the surface can be analyzed clearly.

2) Observing the variation of band edges in photocatalysts during reactions. Through *in-situ* XPS and UPS technologies, the band bending phenomenon, which resulted from electron transfer between the photocatalyst and the solvent due to unequal Fermi levels, could be monitored in photocatalytic experiments.[198,199]

3) Detecting the morphology and surface states of photocatalysts under photocatalytic conditions. The local states like surface potential and the morphology of some active components might be directly observed by *in-situ* electron microscopy. Thus, the charge transfer mechanism and reaction kinetics could be explained.

In a word, we hope this section could help those researchers, especially those who've only just started engaging in the PDRM area, to select reasonably advanced techniques for predicting some catalytic performance of proposed photocatalysts for PDRM application, investigating the properties of as-designed semiconductor photocatalysts, and even proving their elaborate ideas. In addition, some *in-situ* characterization methods with great potential and multifunction should be fully utilized in the PDRM area for getting landmark breakthroughs.

7. Conclusion and outlook

CH₄ as a C₁ compound is an important factor in the energy transition from fossil fuels to sustainable energy. Meanwhile, DRM technology is able to effectively decrease the massive greenhouse gas (CO₂ and CH₄) and attain carbon neutralization. However, the thermodynamic stability of CH₄ and CO₂ is the biggest obstacle to achieve efficient CH₄ conversion. As mentioned above, different thermal-driven catalytic systems have been continuously developed to overcome this thermodynamic disadvantage. Nonetheless, the high temperature for initiating the CH₄ conversion process always inevitably causes energy consumption and catalyst deactivation. Fortunately, the emergence of the environmentally friendly photocatalysis technique gradually reduces the harsh reaction conditions during conventional DRM, indicating that carbon neutralization is possible. One of the great problems of PDRM is low efficiency and apparent quantum yield (AQY). Although the highest AQY for PDRM achieved 60.0% on Pt/black TiO₂, most photocatalysts have less than 10.0% AQY, meaning that PDRM does not meet the requirements of commercialization and industrialization yet.[200] Charge transfer kinetics is one of the main factors, which determine AQY. In this context, it has been confirmed that constructing a built-in electric field in photocatalysts can play a pivotal role in manipulating

the PDRM efficiency via regulating charge transfer/separation dynamics. Many breakthroughs have been made in this area, some typical examples are listed in **Table 2**. However, there are still some challenging obstacles and deficiencies to overcome, as discussed below.

1) Fabrication of new built-in electric field-assisted photocatalysts for PDRM. In the past several decades, the research on constructing photocatalysts with built-in electric fields are carried out gradually for engaging reactions producing the desirable chemicals and energy carriers (e.g. H₂ production via water splitting and CO generation via CO₂ photoreduction). However, catalysts with built-in electric fields are rarely used for emerging reactions like PDRM. One possible reason is the harsh requirement of energy band structures for PDRM application, meaning that photocatalysts should excite photogenerated charges with high redox ability to complete CO₂ reduction and CH₄ oxidation simultaneously. Many efforts in energy band engineering have been conducted to design photocatalysts with suitable energy bands and rapid charge separation behavior. But it is seemingly impractical to test all the possible candidates experimentally to explore their energy band and Fermi level in detail. In order to deal with this obstacle, DFT calculations have been engaged in exploring the electronic structure of semiconductors and metals to provide theoretical support for screening reasonable photocatalysts with strong redox potential and high charge transfer ability. What's more, machine learning (ML) technology as an emergent tactic can offer detailed data of different materials to estimate parameters, such as band gap, CB, VB, and electronic conductivity. It is expected that with the development of materials databases, the ML method will play an important role in the discovery and design of photocatalysts for the PDRM reaction.

2) Development of advanced reactors. Designing or updating reactors is equally

meaningful as the development of photocatalysts. It has been proved that flow reaction vectors are more effective than batch reaction vectors for different photocatalytic applications. The unique advantages of flow reactors include the real-time regulation of reactant pressure to make sure selectivity and timely emission of products to avoid the deactivation of catalysts. In consideration of the latent cost and safety issues during DRM reaction, the design of photocatalytic gas-solid reactors should refer to the mature flow systems in conventional thermal-driven catalysis. What's more, introducing certain external devices for enhancing built-in electric fields can also be considered to fully make use of the advantage of electric field-assisted photocatalysts. Taking the ferroelectric photocatalyst as an example, the variation of polarization states can adjust the adsorption and desorption ability of reactants and products over the ferroelectric photocatalysts surface, respectively. Thus, periodically controlling the surface state and thus changing the direction of electric fields via external stimulation, the activity and selectivity during PDRM will be easily controlled in ferroelectric-assisted photocatalytic systems. In brief, more efforts are needed to develop and update reactors for realizing the industrialization of PDRM at an early date.

3) Understanding of enhancement and reaction mechanisms of PDRM. Compared with other photocatalytic reactions like water splitting, CO₂ reduction, and degradation, PDRM is a relatively new application. The understanding of the PDRM reaction mechanism including photophysics and photochemistry theory is limited and simple. Much research did not in-depth clarify the role of photons in the dissociation of reactants. Besides, the intermediates and local reaction pathways of PDRM need to be furtherly explored because the surface states of photocatalysts could be influenced by built-in electric fields. In addition to the PDRM reaction

mechanism, more direct evidence should be provided to show the impact of the built-in electric field on charge separation and transfer routes. Some authors claimed that photoexcited electron-hole pairs would migrate to different active sites with the assistance of an electric field. But most early works only theoretically simulate the charge transfer process instead of directly determining the migration pathways through the variation of surface potential or triggering reduction and oxidation at different reactive sites. In order to investigate reaction and enhancement mechanisms in electric field-assisted photocatalytic systems, some advanced characterization methods involving, but not limited to, *in-situ* X-ray photoelectron spectroscopy (XPS), *in-situ* Fourier transform infrared spectroscopy (FT-IR), *in-situ* electron paramagnetic resonance (ESR) spectroscopy, piezoresponse force microscopy (PMF), and Kelvin probe force microscope (KPFM) analysis should be utilized in PDRM field. By means of *in-situ* characterizations, some in-depth understanding of PDRM over photocatalysts with the built-in electric field might be proposed in the future.

It is undeniable that PDRM technology, which is far from industrial applications, is still at a very early stage. However, this environmental-friendly methane conversion route would be rapidly developed owing to the advances in characterization techniques and chemical synthesis strategies. Thus, PDRM will play an important role in green chemistry and carbon neutrality. Additionally, some photocatalysts with enhanced charge separation/transfer kinetics adjusted by electric field have exhibited great potential in highly efficient PDRM. Therefore, it could be expected that more studies of built-in electric field-assisted PDRM will be carried out in the coming decades.

Table 2 Different thermal-/photo(thermal)-catalysts for DRM reaction

Catalysts	Type	Reaction conditions	Catalytic performance	Ref.
Rh-Ni/Al ₂ O ₃	Thermal catalyst	Catalyst: 100 mg Total gas flow rate: 0.83 N cm ³ ·s ⁻¹ Gas hourly space velocity (GHSV) = 6000 h ⁻¹ CH ₄ /CO ₂ /He = 20/20/60 Temperature: 973K Pressure: 1 atm	CO ₂ conversion: ~ 85% CH ₄ conversion: ~ 65% H ₂ /CO: ~ 0.85	[58]
Pt/CeO ₂	Photocatalyst	Catalyst: 50 mg Light source: 500 W Xe lamp total gas flow rate: 120.5 ml·min ⁻¹ CH ₄ /CO ₂ /Ar = 10/10/80	Unit: mmol·min ⁻¹ ·g ⁻¹ CO ₂ conversion: ~ 3.2 CH ₄ conversion: ~ 2.7 H ₂ : 5.7 CO: 6.0	[83]
BaZr _{0.05} Ti _{0.95} O ₃	Ferroelectric non-thermal plasmonic catalyst	Catalyst: 0.5 g DC pulse voltages: 13 kV frequency = 20,000 Hz Discharge gap = 5 mm. total gas flow rate: 100 mL·min ⁻¹ GHSV: 8500 h ⁻¹ CH ₄ /CO ₂ = 1/1	CO ₂ conversion: 79.0% conversion CH ₄ conversion: 84.2% H ₂ selectivity: 87.5% CO selectivity: 69.2%	[124]
BaTiO ₃ /Fe ₂ O ₃	Ferroelectric photocatalyst	Hg lamp 125 W CO ₂ /CH ₄ /He = 45/45/10 Pressure: 40 psia Temperature: 30 ± 5 °C	CO ₂ conversion: 22.3%	
Pt/TaN	Ferroelectric photocatalyst	Catalyst: 0.10 g Light source: Xe lamp Total flow rate: 20.0mL/min CH ₄ /CO ₂ = 1/1 Temperature: 500 °C	Unit: μmol·min ⁻¹ ·g ⁻¹ CO ₂ conversion: ~ 700 CH ₄ conversion: ~ 550 H ₂ : 1100 CO: 1200	[126]
Ti ₃ C ₂ /TiO ₂ /g-C ₃ N ₄	Type-II heterojunction photocatalyst	Catalyst: 100 mg Light source: 35 W Xenon lamp light intensity: 20 mW·cm ⁻² CO ₂ /CH ₄ : 2/1 (10/5 mL·min ⁻¹) Pressure: 0.10 bars	Unit: μmol·g ⁻¹ ·h ⁻¹ H ₂ : 45.69 CO: 87.34 CO selectivity: 65.6% H ₂ selectivity: 34.40%	[143]
TiO ₂ -TiC/g-C ₃ N ₄	All-solid-state Z-scheme heterojunction photocatalyst	Catalyst: 50 mg Light source: Xe lamp Light intensity: 335 mW·cm ⁻² Pressure: 40 kPa CH ₄ /CO ₂ = 1/2 Temperature: room temperature	Unit: μmol·g ⁻¹ ·h ⁻¹ CO: 11.3 H ₂ : 2.15	[148]
CoAl-LDH/g-C ₃ N ₄ /Ti ₃ AlC ₂	Direct Z-scheme heterojunction photocatalysts	Catalyst: 100 mg Light source: 35 W Xe lamp Light intensity: 20 mW·cm ⁻² total flow rate: 20 ml·min ⁻¹ CH ₄ /CO ₂ = 1/1	Unit: μmol·g ⁻¹ ·h ⁻¹ CO: 22.5 H ₂ : 4.74	[150]

Pressure: 0.3 bars				
Ag/TiO ₂	Plasmonic	Catalyst: 100 mg	Unit: $\mu\text{mol}\cdot\text{g}^{-1}\cdot\text{h}^{-1}$	[175]
	Photocatalyst	Light source: Xe lamp	CO: 1149	
		Light intensity: 84.2 $\text{mW}\cdot\text{cm}^{-2}$	C ₂ H ₄ : 686	
		CO ₂ /CH ₄ /Ar = 7.5/7.5/85		
Pressure: 2 MPa				
Pt/Au-SiO ₂	Plasmonic	Catalyst: 20 mg	Unit: $\mu\text{mol}\cdot\text{g}^{-1}\cdot\text{h}^{-1}$	[176]
	photocatalyst	Light source: Xe lamp	CO ₂ conversion: ~68.6	
		Total flow rate: 20.0 $\text{mL}\cdot\text{min}^{-1}$	CH ₄ conversion: ~55.0	
		CO ₂ /CH ₄ = 1/1	CO: ~120	
		H ₂ : ~90		

Declaration of Competing Interest

The authors declare no competing interest.

Acknowledgments

This work received financial support from the National Natural Science Foundation of China (21902116) and Scientific Research Foundation of Technology Department of Liaoning Province of China (2022-MS-379). Support from the Ministerio de Ciencia e Innovación (MICINN) de España (PID2019-104171RB-I00, TED2021-129237B-I00) is gratefully acknowledged.

References

- [1] X. Zhao, B. Joseph, J. Kuhn, S. Ozcan, *iScience*, **2020**, *23*, 101082.
- [2] P. Schwach, X. Pan, X. Bao, *Chem. Rev.*, **2017**, *117*, 8497.
- [3] N. J. Gunsalus, A. Koppaka, S. H. Park, S. M. Bischof, B. G. Hashiguchi, R. A. Periana, *Chem. Rev.*, **2017**, *117*, 8521.
- [4] L. Yuliati, H. Yoshida, *Chem. Soc. Rev.*, **2008**, *37*, 1592.

- [5] S. Lin, J. Wang, Y. Mi, S. Yang, Z. Wang, W. Liu, D. Wu, H. Peng, *Chinese J. Catal.*, **2021**, *42*, 1808.
- [6] J. Tian, H. Li, X. Zeng, Z. Wang, J. Huang, C. Zhao, *Chinese J. Catal.*, **2019**, *40*, 1395.
- [7] D. Bahnemann, *Sol. Energy*, **2004**, *77*, 445.
- [8] H. Kato, A. Kudo, *J. Phys. Chem. B*, **2001**, *105*, 4285.
- [9] C. He, S. Wu, Q. Li, M. Li, J. Li, L. Wang, J. Zhang, *Chem*, **2023**, DOI 10.1016/j.chempr.2023.06.021.
- [10] S. Shoji, X. Peng, A. Yamaguchi, R. Watanabe, C. Fukuhara, Y. Cho, T. Yamamoto, S. Matsumura, M. Yu, S. Ishii, T. Fujita, H. Abe, M. Miyauchi, *Nat. Catal.*, **2020**, *3*, 148.
- [11] J. Wen, J. Xie, X. Chen, X. Li, *Appl. Surf. Sci.*, **2017**, *391*, 72.
- [12] H. Tong, S. Ouyang, Y. Bi, N. Umezawa, M. Oshikiri, J. Ye, *Adv. Mater.*, **2012**, *24*, 229.
- [13] B. Dai, J. Fang, Y. Yu, M. Sun, H. Huang, C. Lu, J. Kou, Y. Zhao, Z. Xu, *Adv. Mater.*, **2020**, *32*, 1906361.
- [14] Z. Zhao, H. Tan, H. Zhao, Y. Lv, L. J. Zhou, Y. Song, Z. Sun, *Chem. Commun.*, **2014**, *50*, 2755.
- [15] P. Jiménez-Calvo, V. Caps, V. Keller, *Renew. Sustain. Energy Rev.*, **2021**, *149*, 111095.
- [16] L. Liu, S. Ouyang, J. Ye, *Angew. Chemie Int. Ed.*, **2013**, *52*, 6689.
- [17] X. Xu, F. Luo, W. Tang, J. Hu, H. Zeng, Y. Zhou, *Adv. Funct. Mater.*, **2018**, *28*, 1804055.
- [18] L. Yin, M. Zhao, H. Hu, J. Ye, D. Wang, *Chinese J. Catal.*, **2017**, *38*, 1307.
- [19] J. Tan, X. Wang, W. Hou, X. Zhang, L. Liu, J. Ye, D. Wang, *J. Alloys Compd.*, **2019**, *792*, 918.
- [20] M. Ye, X. Wang, E. Liu, J. Ye, D. Wang, *ChemSusChem*, **2018**, *11*, 1606.

- [21] J. Li, Z. Wang, H. Chen, Q. Zhang, H. Hu, L. Liu, J. Ye, D. Wang, *Catal. Sci. Technol.*, **2021**, *11*, 4953.
- [22] P. Li, L. Liu, W. An, H. Wang, H. Guo, Y. Liang, W. Cui, *Appl. Catal. B Environ.*, **2020**, *266*, 118618.
- [23] A. Meng, L. Zhang, B. Cheng, J. Yu, *Adv. Mater.*, **2019**, *31*, 1807660.
- [24] K. Wu, J. Xiong, Y. Sun, J. Wu, M. Fu, D. Ye, *J. Hazard. Mater.*, **2022**, *428*, 128172.
- [25] X. Xu, L. Xiao, Y. Jia, Z. Wu, F. Wang, Y. Wang, N. O. Haugen, H. Huang, *Energy Environ. Sci.*, **2018**, *11*, 2198.
- [26] Y. Cho, S. Kim, B. Park, C. L. Lee, J. K. Kim, K. S. Lee, I. Y. Choi, J. K. Kim, K. Zhang, S. H. Oh, J. H. Park, *Nano Lett.*, **2018**, *18*, 4257.
- [27] F. Dong, Z. Zhao, T. Xiong, Z. Ni, W. Zhang, Y. Sun, W. Ho, *ACS Appl. Mater. Interfaces*, **2013**, *5*, 11392.
- [28] X. Zhang, X. Wang, D. Wang, J. Ye, *ACS Appl. Mater. Interfaces*, **2019**, *11*, 5623.
- [29] Q. Wang, L. Dong, M. Li, H. Lu, G. Wei, Y. Qu, G. Wang, *Adv. Funct. Mater.*, **2022**, *32*, 2207330.
- [30] X. Yang, L. Tian, X. Zhao, H. Tang, Q. Liu, G. Li, *Appl. Catal. B Environ.*, **2019**, *244*, 240.
- [31] J. Low, J. Yu, M. Jaroniec, S. Wageh, A. A. Al-Ghamdi, *Adv. Mater.*, **2017**, *29*, 1601694.
- [32] H. S. Moon, K. Hsiao, M. Wu, Y. Yun, Y. Hsu, K. Yong, *Adv. Mater.*, **2022**, 2200172.
- [33] Y. Li, Y. Yan, Y. Li, H. Zhang, D. Li, D. Yang, *CrystEngComm*, **2015**, *17*, 1833.
- [34] S. Xie, H. Zhang, G. Liu, X. Wu, J. Lin, Q. Zhang, Y. Wang, *Chinese J. Catal.*, **2020**, *41*, 1125.

- [35] Y. Lu, X. Jia, Z. Ma, Y. Li, S. Yue, X. Liu, J. Zhang, *Adv. Funct. Mater.*, **2022**, *32*, 2203638.
- [36] M. Zhang, L. Tang, A. Duan, Y. Zhang, F. Xiao, Y. Zhu, J. Wang, C. Feng, N. Yin, *Chem. Eng. J.*, **2023**, *452*, 139068.
- [37] L. Zhou, Z. Liu, Z. Guan, B. Tian, L. Wang, Y. Zhou, Y. Zhou, J. Lei, J. Zhang, Y. Liu, *Appl. Catal. B Environ.*, **2020**, *263*, 118326.
- [38] K. Wittich, M. Krämer, N. Bottke, S. A. Schunk, *ChemCatChem*, **2020**, *12*, 2130.
- [39] C. D. Thomas, A. Cameron, R. E. Green, M. Bakkenes, L. J. Beaumont, Y. C. Collingham, B. F. N. Erasmus, M. F. de Siqueira, A. Grainger, L. Hannah, L. Hughes, B. Huntley, A. S. van Jaarsveld, G. F. Midgley, L. Miles, M. A. Ortega-Huerta, A. Townsend Peterson, O. L. Phillips, S. E. Williams, *Nature*, **2004**, *427*, 145.
- [40] C. Hepburn, E. Adlen, J. Beddington, E. A. Carter, S. Fuss, N. Mac Dowell, J. C. Minx, P. Smith, C. K. Williams, *Nature*, **2019**, *575*, 87.
- [41] P. Gronchi, P. Centola, R. D. Rosso, *Appl. Catal. A Gen.*, **1997**, *152*, 83.
- [42] B. Christian Enger, R. Lødeng, A. Holmen, *Appl. Catal. A Gen.*, **2008**, *346*, 1.
- [43] C. Papadopoulou, H. Matralis, X. Verykios, in *Catal. Altern. Energy Gener.*, **2012**, 57–127.
- [44] A. Álvarez, M. Borges, J. J. Corral-Pérez, J. G. Olcina, L. Hu, D. Cornu, R. Huang, D. Stoian, A. Urakawa, *ChemPhysChem*, **2017**, *18*, 3135.
- [45] L. F. Bobadilla, V. Garcilaso, M. A. Centeno, J. A. Odriozola, *ChemSusChem*, **2017**, *10*, 1193.
- [46] S. Xie, Q. Zhang, G. Liu, Y. Wang, *Chem. Commun.*, **2016**, *52*, 35.

- [47] M. F. Mark, W. F. Maier, F. Mark, *Chem. Eng. Technol.*, **1997**, *20*, 361.
- [48] Y. Kathiraser, U. Oemar, E. T. Saw, Z. Li, S. Kawi, *Chem. Eng. J.*, **2015**, *278*, 62.
- [49] E. le Saché, T. R. Reina, *Prog. Energy Combust. Sci.*, **2022**, *89*, 100970.
- [50] R. O. da Fonseca, R. C. Rabelo-Neto, R. C. C. Simões, L. V. Mattos, F. B. Noronha, *Int. J. Hydrogen Energy*, **2020**, *45*, 5182.
- [51] B. Faroldi, J. Múnera, J. M. Falivene, I. R. Ramos, Á. G. García, L. T. Fernández, S. G. Carrazán, L. Cornaglia, *Int. J. Hydrogen Energy*, **2017**, *42*, 16127.
- [52] J. Yang, J. Wang, J. Zhao, Y. Bai, H. Du, Q. Wang, B. Jiang, H. Li, *J. CO₂ Util.*, **2022**, *57*, 101893.
- [53] C. Carrara, J. Múnera, E. A. Lombardo, L. M. Cornaglia, *Top. Catal.*, **2008**, *51*, 98.
- [54] J. Park, T. Chang, *Catal. Letters*, **2019**, *149*, 3148.
- [55] I. de Dios García, A. Stankiewicz, H. Nigar, *Catal. Today*, **2021**, *362*, 72.
- [56] K. Nagaoka, *Appl. Catal. A Gen.*, **2004**, *268*, 151.
- [57] B. Pawelec, S. Damyanova, K. Arishtirova, J. L. G. Fierro, L. Petrov, *Appl. Catal. A Gen.*, **2007**, *323*, 188.
- [58] M. García-Diéguez, I. S. Pieta, M. C. Herrera, M. A. Larrubia, L. J. Alemany, *Catal. Today*, **2011**, *172*, 136.
- [59] B. Steinhauer, M. R. Kasireddy, J. Radnik, A. Martin, *Appl. Catal. A Gen.*, **2009**, *366*, 333.
- [60] F. Menegazzo, M. Signoretto, F. Pinna, P. Canton, N. Pernicone, *Appl. Catal. A Gen.*, **2012**, *439–440*, 80.
- [61] A. Abdulrasheed, A. A. Jalil, Y. Gambo, M. Ibrahim, H. U. Hambali, M. Y. Shahul

- Hamid, *Renew. Sustain. Energy Rev.*, **2019**, *108*, 175.
- [62] O. Muraza, A. Galadima, *Int. J. Energy Res.*, **2015**, *39*, 1196.
- [63] Y. Gao, J. Jiang, Y. Meng, F. Yan, A. Aihemaiti, *Energy Convers. Manag.*, **2018**, *171*, 133.
- [64] G. Jones, J. Jakobsen, S. Shim, J. Kleis, M. Andersson, J. Rossmeisl, F. Abildpedersen, T. Bligaard, S. Helveg, B. Hinnemann, *J. Catal.*, **2008**, *259*, 147.
- [65] H. Song, X. Meng, Z. jun Wang, H. Liu, J. Ye, *Joule*, **2019**, *3*, 1606.
- [66] A. Tavasoli, A. Gouda, T. Zähringer, Y. F. Li, H. Quaid, C. J. Viasus Perez, R. Song, M. Sain, G. Ozin, *Nat. Commun.*, **2023**, *14*, 1435.
- [67] J. Barber, *Chem. Soc. Rev.*, **2009**, *38*, 185.
- [68] X. Li, C. Wang, J. Tang, *Nat. Rev. Mater.*, **2022**, *7*, 617–632.
- [69] S. Zhang, P. Gu, R. Ma, C. Luo, T. Wen, G. Zhao, W. Cheng, X. Wang, *Catal. Today*, **2019**, *335*, 65.
- [70] Fujishima A, *Nature*, **1972**, *238*, 37.
- [71] M. Kushida, A. Yamaguchi, M. Miyauchi, *J. Energy Chem.*, **2022**, *71*, 562.
- [72] B. Han, W. Wei, L. Chang, P. Cheng, Y. H. Hu, *ACS Catal.*, **2016**, *6*, 494.
- [73] A. Ali Khan, M. Tahir, *Ind. Eng. Chem. Res.*, **2021**, *60*, 16201.
- [74] H. Tong, S. Ouyang, Y. Bi, N. Umezawa, M. Oshikiri, J. Ye, *Adv. Mater.*, **2012**, *24*, 229.
- [75] A. L. Linsebigler, G. Lu, J. T. Yates, *Chem. Rev.*, **1995**, *95*, 735.
- [76] N. Huang, T. Su, Z. Qin, H. Ji, *ChemistrySelect*, **2022**, *7*, e202203873.
- [77] A. A. Khan, M. Tahir, Z. Y. Zakaria, *J. Environ. Chem. Eng.*, **2021**, *9*, 105244.
- [78] A. Ali Khan, M. Tahir, *Ind. Eng. Chem. Res.*, **2021**, *60*, 16201.

- [79] A. Ali Khan, M. Tahir, *ACS Appl. Energy Mater.*, **2022**, *5*, 784.
- [80] S. Wu, Y. Li, Q. Hu, J. Wu, Q. Zhang, *ACS Sustain. Chem. Eng.*, **2021**, *9*, 11635.
- [81] R. R. Ikreedeegh, M. Tahir, *Fuel*, **2021**, *305*, 121558.
- [82] M. Mao, Q. Zhang, Y. Yang, Y. Li, H. Huang, Z. Jiang, Q. Hu, X. Zhao, *Green Chem.*, **2018**, *20*, 2857.
- [83] Y. Tang, Y. Li, V. Fung, D. Jiang, W. Huang, S. Zhang, Y. Iwasawa, T. Sakata, L. Nguyen, X. Zhang, A. I. Frenkel, F. Tao, *Nat. Commun.*, **2018**, *9*, 1231.
- [84] T. Ikuno, J. Zheng, A. Vjunov, M. Sanchez-Sanchez, M. A. Ortuño, D. R. Pahls, J. L. Fulton, D. M. Camaioni, Z. Li, D. Ray, B. L. Mehdi, N. D. Browning, O. K. Farha, J. T. Hupp, C. J. Cramer, L. Gagliardi, J. A. Lercher, *J. Am. Chem. Soc.*, **2017**, *139*, 10294.
- [85] X. Cui, H. Li, Y. Wang, Y. Hu, L. Hua, H. Li, X. Han, Q. Liu, F. Yang, L. He, X. Chen, Q. Li, J. Xiao, D. Deng, X. Bao, *Chem*, **2018**, *4*, 1902.
- [86] Y. Chen, M. Li, Z. Li, F. Liu, G. Song, S. Kawi, *Energy Convers. Manag.*, **2022**, *265*, 115744.
- [87] Y. Sun, W. Zhang, Q. Wang, N. Han, A. Núñez-Delgado, Y. Cao, W. Si, F. Wang, S. Liu, *Environ. Res.*, **2021**, *202*, 111684.
- [88] X. Hou, Y. Cai, D. Zhang, L. Li, X. Zhang, Z. Zhu, L. Peng, Y. Liu, J. Qiao, *J. Mater. Chem. A*, **2019**, *7*, 3197.
- [89] Y. Liu, X. Li, H. He, S. Yang, G. Jia, S. Liu, *J. Colloid Interface Sci.*, **2021**, *599*, 23.
- [90] J. Guo, X. Zhang, X.-Y. Dao, W.-Y. Sun, *ACS Appl. Nano Mater.*, **2020**, *3*, 2625.
- [91] R. Li, F. Liu, Y. Zhang, M. Guo, D. Liu, *ACS Appl. Mater. Interfaces*, **2020**, *12*, 44578.
- [92] D. Lee, S. Moru, R. Bhosale, W. Jo, S. Tonda, *Appl. Surf. Sci.*, **2022**, *599*, 153973.

- [93] A. Muhammad, M. Tahir, S. S. Al-Shahrani, A. Mahmood Ali, S. U. Rather, *Appl. Surf. Sci.*, **2020**, *504*, 144177.
- [94] J. Horlyck, C. Lawrey, E. C. Lovell, R. Amal, J. Scott, *Chem. Eng. J.*, **2018**, *352*, 572.
- [95] M. Xu, X. Hu, S. Wang, J. Yu, D. Zhu, J. Wang, *J. Catal.*, **2019**, *377*, 652.
- [96] H. Zhang, T. Wang, J. Wang, H. Liu, T. D. Dao, M. Li, G. Liu, X. Meng, K. Chang, L. Shi, T. Nagao, J. Ye, *Adv. Mater.*, **2016**, *28*, 3703.
- [97] X. Feng, D. Liu, B. Yan, M. Shao, Z. Hao, G. Yuan, H. Yu, Y. Zhang, *Angew. Chemie*, **2021**, *133*, 18700.
- [98] Z. Li, J. Liu, Y. Zhao, G. I. N. Waterhouse, G. Chen, R. Shi, X. Zhang, X. Liu, Y. Wei, X.-D. Wen, L. Wu, C. Tung, T. Zhang, *Adv. Mater.*, **2018**, *30*, 1800527.
- [99] C. Song, X. Liu, M. Xu, D. Masi, Y. Wang, Y. Deng, M. Zhang, X. Qin, K. Feng, J. Yan, J. Leng, Z. Wang, Y. Xu, B. Yan, S. Jin, D. Xu, Z. Yin, D. Xiao, D. Ma, *ACS Catal.*, **2020**, *10*, 10364.
- [100] C. Song, Z. Wang, Z. Yin, D. Xiao, D. Ma, *Chem Catal.*, **2022**, *2*, 52.
- [101] Q. Hu, Y. Li, J. Wu, Y. Hu, H. Cao, Y. Yang, *Adv. Energy Mater.*, **2023**, *13*, 2300071.
- [102] M. J. Kale, T. Avanesian, P. Christopher, *ACS Catal.*, **2014**, *4*, 116.
- [103] P. Christopher, M. Moskovits, *Annu. Rev. Phys. Chem.*, **2017**, *68*, 379.
- [104] M. J. Kale, P. Christopher, *Science*, **2015**, *349*, 587.
- [105] S. Linic, U. Aslam, C. Boerigter, M. Morabito, *Nat. Mater.*, **2015**, *14*, 567.
- [106] U. Aslam, V. G. Rao, S. Chavez, S. Linic, *Nat. Catal.*, **2018**, *1*, 656.
- [107] L. Meng, Z. Chen, Z. Ma, S. He, Y. Hou, H. Li, R. Yuan, X. Huang, X. Wang, X. Wang, J. Long, *Energy Environ. Sci.*, **2018**, *11*, 294.

- [108] B. Dai, Y. Chen, S. Hao, H. Huang, J. Kou, C. Lu, Z. Lin, Z. Xu, *J. Phys. Chem. Lett.*, **2020**, *11*, 7407.
- [109] M. Wang, B. Wang, F. Huang, Z. Lin, *Angew. Chemie Int. Ed.*, **2019**, *58*, 7526.
- [110] Q. Shi, M. Zhang, Z. Zhang, Y. Li, Y. Qu, Z. Liu, J. Yang, M. Xie, W. Han, *Nano Energy*, **2020**, *69*, 104448.
- [111] Y. Lei, Z. Jia, H. Hu, L. Liu, J. Ye, D. Wang, *Catalysts*, **2022**, *12*, 1323.
- [112] N. Ma, N. Tanen, A. Verma, Z. Guo, T. Luo, H. (Grace) Xing, D. Jena, *Appl. Phys. Lett.*, **2016**, *109*, 212101.
- [113] Y. Zhao, J. Qiao, Z. Yu, P. Yu, K. Xu, S. P. Lau, W. Zhou, Z. Liu, X. Wang, W. Ji, Y. Chai, *Adv. Mater.*, **2017**, *29*, 1604230.
- [114] P. S. Bednyakov, T. Sluka, A. K. Tagantsev, D. Damjanovic, N. Setter, *Sci. Rep.*, **2015**, *5*, 15819.
- [115] X. Liu, F. Zhang, P. Long, T. Lu, H. Zeng, Y. Liu, R. L. Withers, Y. Li, Z. Yi, *Adv. Mater.*, **2018**, *30*, 1801619.
- [116] H. Li, X. Quan, S. Chen, H. Yu, *Appl. Catal. B Environ.*, **2017**, *209*, 591.
- [117] H. Simons, A. B. Haugen, A. C. Jakobsen, S. Schmidt, F. Stöhr, M. Majkut, C. Detlefs, J. E. Daniels, D. Damjanovic, H. F. Poulsen, *Nat. Mater.*, **2018**, *17*, 814.
- [118] B. Dai, Y. Yu, Y. Chen, H. Huang, C. Lu, J. Kou, Y. Zhao, Z. Xu, *Adv. Funct. Mater.*, **2019**, *29*, 1970105.
- [119] X. Chen, Y. Li, X. Pan, D. Cortie, X. Huang, Z. Yi, *Nat. Commun.*, **2016**, *7*, 12273.
- [120] W. Song, P. A. Salvador, G. S. Rohrer, *ACS Appl. Mater. Interfaces*, **2018**, *10*, 41450.
- [121] O. Kwon, D. Seol, D. Lee, H. Han, I. Lindfors-Vrejoiu, W. Lee, S. Jesse, H. N. Lee, S.

- V. Kalinin, M. Alexe, Y. Kim, *Adv. Mater.*, **2018**, *30*, 1703675.
- [122] J. He, Y. Zhao, S. Jiang, S. Song, *Sol. RRL*, **2021**, *5*, 2000446.
- [123] W.-C. Chung, M.-B. Chang, *Energy Convers. Manag.*, **2016**, *124*, 305.
- [124] N. P. Zangeneh, S. Sharifnia, E. Karamian, *Environ. Sci. Pollut. Res.*, **2020**, *27*, 5912.
- [125] H. Liu, H. Song, W. Zhou, X. Meng, J. Ye, *Angew. Chemie Int. Ed.*, **2018**, *57*, 16781.
- [126] Y. Cui, J. Briscoe, S. Dunn, *Chem. Mater.*, **2013**, *25*, 4215.
- [127] C. Paillard, X. Bai, I. C. Infante, M. Guennou, G. Geneste, M. Alexe, J. Kreisel, B. Dkhil, *Adv. Mater.*, **2016**, *28*, 5153.
- [128] F. Chen, H. Huang, L. Guo, Y. Zhang, T. Ma, *Angew. Chemie*, **2019**, *131*, 10164.
- [129] H. Kanda, N. Shibayama, A. J. Huckaba, Y. Lee, S. Paek, N. Klipfel, C. Roldán-Carmona, V. I. E. Queloz, G. Grancini, Y. Zhang, M. Abuhelaiqa, K. T. Cho, M. Li, M. D. Mensi, S. Kinge, M. K. Nazeeruddin, *Energy Environ. Sci.*, **2020**, *13*, 1222.
- [130] H. Huang, S. Tu, X. Du, Y. Zhang, *J. Colloid Interface Sci.*, **2018**, *509*, 113.
- [131] C. Peng, G. Reid, H. Wang, P. Hu, *J. Chem. Phys.*, **2017**, *147*, 030901.
- [132] Z. Du, C. Petru, X. Yang, F. Chen, S. Fang, F. Pan, Y. Gang, H. Zhou, Y. H. Hu, Y. Li, *J. CO₂ Util.*, **2023**, *67*, 102317.
- [133] K. T. Ranjit, B. Viswanathan, *J. Photochem. Photobiol. A Chem.*, **1997**, *108*, 79.
- [134] H. Zhou, Y. Qu, T. Zeid, X. Duan, *Energy Environ. Sci.*, **2012**, *5*, 6732.
- [135] H. Wang, L. Zhang, Z. Chen, J. Hu, S. Li, Z. Wang, J. Liu, X. Wang, *Chem. Soc. Rev.*, **2014**, *43*, 5234.
- [136] S. J. A. Moniz, S. A. Shevlin, D. J. Martin, Z.-X. Guo, J. Tang, *Energy Environ. Sci.*, **2015**, *8*, 731.

- [137] W. Shi, N. Chopra, *Nanomater. Energy*, **2013**, *2*, 158.
- [138] J. K. Hyun, S. Zhang, L. J. Lauhon, *Annu. Rev. Mater. Res.*, **2013**, *43*, 451.
- [139] S. J. Hong, S. Lee, J. S. Jang, J. S. Lee, *Energy Environ. Sci.*, **2011**, *4*, 1781.
- [140] L. Huang, H. Xu, Y. Li, H. Li, X. Cheng, J. Xia, Y. Xu, G. Cai, *Dalt. Trans.*, **2013**, *42*, 8606.
- [141] C. Pan, J. Xu, Y. Wang, D. Li, Y. Zhu, *Adv. Funct. Mater.*, **2012**, *22*, 1518.
- [142] A. A. Khan, M. Tahir, *Appl. Catal. B Environ.*, **2021**, *285*, 119777.
- [143] H. Tada, T. Mitsui, T. Kiyonaga, T. Akita, K. Tanaka, *Nat. Mater. 2006 510*, **2006**, *5*, 782.
- [144] X. Li, X. Yan, X. Lu, S. Zuo, Z. Li, C. Yao, C. Ni, *J. Catal.*, **2018**, *357*, 59.
- [145] P. Zhou, J. Yu, M. Jaroniec, *Adv. Mater.*, **2014**, *26*, 4920.
- [146] H. Li, H. Yu, X. Quan, S. Chen, Y. Zhang, *ACS Appl. Mater. Interfaces*, **2016**, *8*, 2111.
- [147] Z. Li, Y. Mao, Y. Huang, D. Wei, M. Chen, Y. Huang, B. Jin, X. Luo, Z. Liang, *Catal. Sci. Technol.*, **2022**, *12*, 2804.
- [148] Q. Xu, L. Zhang, J. Yu, S. Wageh, A. A. Al-Ghamdi, M. Jaroniec, *Mater. Today*, **2018**, *21*, 1042.
- [149] M. Tahir, R. Mansoor, *J. Alloys Compd.*, **2023**, *947*, 169457.
- [150] J. Fu, Q. Xu, J. Low, C. Jiang, J. Yu, *Appl. Catal. B Environ.*, **2019**, *243*, 556.
- [151] Z. Wang, Y. Chen, L. Zhang, B. Cheng, J. Yu, J. Fan, *J. Mater. Sci. Technol.*, **2020**, *56*, 143.
- [152] W. Wang, G. Huang, J. C. Yu, P. K. Wong, *J. Environ. Sci.*, **2015**, *34*, 232.
- [153] A. Ali Khan, M. Tahir, N. Khan, *Energy Convers. Manag.*, **2023**, *286*, 117021.

- [154] Y. Zhang, M. Xu, W. Zhou, X. Song, X. Liu, J. Zhang, S. Chen, P. Huo, *J. Colloid Interface Sci.*, **2023**, *650*, 1762.
- [155] S. Patial, R. Kumar, P. Raizada, P. Singh, Q. Van Le, E. Lichtfouse, D. Le Tri Nguyen, V. Nguyen, *Environ. Res.*, **2021**, *197*, 111134.
- [156] H. Feng, C. Zhang, M. Luo, Y. Hu, Z. Dong, S. Xue, P. K. Chu, *Nanoscale*, **2022**, *14*, 16303.
- [157] Z. Miao, Q. Wang, Y. Zhang, L. Meng, X. Wang, *Appl. Catal. B Environ.*, **2022**, *301*, 120802.
- [158] S. Gong, X. Teng, Y. Niu, X. Liu, M. Xu, C. Xu, L. Ji, Z. Chen, *Appl. Catal. B Environ.*, **2021**, *298*, 120521.
- [159] A. Meng, B. Cheng, H. Tan, J. Fan, C. Su, J. Yu, *Appl. Catal. B Environ.*, **2021**, *289*, 120039.
- [160] J. Wang, Y. Yu, J. Cui, X. Li, Y. Zhang, C. Wang, X. Yu, J. Ye, *Appl. Catal. B Environ.*, **2022**, *301*, 120814.
- [161] Q. Niu, S. Dong, J. Tian, G. Huang, J. Bi, L. Wu, *ACS Appl. Mater. Interfaces*, **2022**, *14*, 24299.
- [162] J. B. Lee, S. Choi, J. Kim, Y. S. Nam, *Nano Today*, **2017**, *16*, 61.
- [163] P. Zhang, T. Wang, J. Gong, *Adv. Mater.*, **2015**, *27*, 5328.
- [164] S. K. Cushing, J. Li, F. Meng, T. R. Senty, S. Suri, M. Zhi, M. Li, A. D. Bristow, N. Wu, *J. Am. Chem. Soc.*, **2012**, *134*, 15033.
- [165] Q. Zhang, D. Thrithamarassery Gangadharan, Y. Liu, Z. Xu, M. Chaker, D. Ma, *J. Mater.*, **2017**, *3*, 33.

- [166] S. Linic, P. Christopher, D. B. Ingram, *Nat. Mater.*, **2011**, *10*, 911.
- [167] S. J. Lee, A. R. Morrill, M. Moskovits, *J. Am. Chem. Soc.*, **2006**, *128*, 2200.
- [168] I. Thomann, B. A. Pinaud, Z. Chen, B. M. Clemens, T. F. Jaramillo, M. L. Brongersma, *Nano Lett.*, **2011**, *11*, 3440.
- [169] Z. Wang, D. Wang, F. Deng, X. Liu, X. Li, X. Luo, Y. Peng, J. Zhang, J. Zou, L. Ding, L. Zhang, *Chem. Eng. J.*, **2023**, *463*, 142313.
- [170] Z. Liu, W. Hou, P. Pavaskar, M. Aykol, S. B. Cronin, *Nano Lett.*, **2011**, *11*, 1111.
- [171] D. B. Ingram, S. Linic, *J. Am. Chem. Soc.*, **2011**, *133*, 5202.
- [172] X. Li, H. Jiang, C. Ma, Z. Zhu, X. Song, H. Wang, P. Huo, X. Li, *Appl. Catal. B Environ.*, **2021**, *283*, 119638.
- [173] H. Liu, X. Meng, T. D. Dao, H. Zhang, P. Li, K. Chang, T. Wang, M. Li, T. Nagao, J. Ye, *Angew. Chemie Int. Ed.*, **2015**, *54*, 11545.
- [174] N. Li, R. Jiang, Y. Li, J. Zhou, Q. Ma, S. Shen, M. Liu, *ACS Sustain. Chem. Eng.*, **2019**, *7*, 11455.
- [175] H. Song, X. Meng, T. D. Dao, W. Zhou, H. Liu, L. Shi, H. Zhang, T. Nagao, T. Kako, J. Ye, *ACS Appl. Mater. Interfaces*, **2018**, *10*, 408.
- [176] T. Torimoto, H. Horibe, T. Kameyama, K. Okazaki, S. Ikeda, M. Matsumura, A. Ishikawa, H. Ishihara, *J. Phys. Chem. Lett.*, **2011**, *2*, 2057.
- [177] L. Zhang, J. Ran, S. Qiao, M. Jaroniec, *Chem. Soc. Rev.*, **2019**, *48*, 5184.
- [178] D. Liu, Z. Shadike, R. Lin, K. Qian, H. Li, K. Li, S. Wang, Q. Yu, M. Liu, S. Ganapathy, X. Qin, Q. Yang, M. Wagemaker, F. Kang, X. Yang, B. Li, *Adv. Mater.*, **2019**, *31*, 1806620.

- [179] F. Meirer, B. M. Weckhuysen, *Nat. Rev. Mater.*, **2018**, *3*, 324.
- [180] A. Kurlov, X. Huang, E. B. Deeva, P. M. Abdala, A. Fedorov, C. R. Müller, *Nanoscale*, **2020**, *12*, 13086.
- [181] V. De Coster, N. V. Srinath, S. A. Theofanidis, L. Pirro, A. Van Alboom, H. Poelman, M. K. Sabbe, G. B. Marin, V. V. Galvita, *Appl. Catal. B Environ.*, **2022**, *300*, 120720.
- [182] A. Rodriguez-Gomez, R. Pereñiguez, A. Caballero, *J. Phys. Chem. B*, **2018**, *122*, 500.
- [183] S. M. Kim, A. Armutlulu, W.-C. Liao, D. Hosseini, D. Stoian, Z. Chen, P. M. Abdala, C. Copéret, C. Müller, *Catal. Sci. Technol.*, **2021**, *11*, 7563.
- [184] Y. Wang, L. Yao, Y. Wang, S. Wang, Q. Zhao, D. Mao, C. Hu, *ACS Catal.*, **2018**, *8*, 6495.
- [185] J. Wang, G. Wang, B. Cheng, J. Yu, J. Fan, *Chinese J. Catal.*, **2021**, *42*, 56.
- [186] M. Yang, Y. Li, Z. Jin, *Sep. Purif. Technol.*, **2023**, *311*, 123229.
- [187] T. Wang, Z. Jin, *J. Mater. Sci. Technol.*, **2023**, *155*, 132.
- [188] J. Zhao, Z. Xiong, J. Wang, Y. Qiu, Y. Zhao, P. Liu, J. Zhang, *Mater. Chem. Front.*, **2022**, *6*, 3205.
- [189] F. Zhang, Z. Liu, S. Zhang, N. Akter, R. M. Palomino, D. Vovchok, I. Orozco, D. Salazar, J. A. Rodriguez, J. Llorca, J. Lee, D. Kim, W. Xu, A. I. Frenkel, Y. Li, T. Kim, S. D. Senanayake, *ACS Catal.*, **2018**, *8*, 3550.
- [190] C. P. Huang, C. Dong, Z. Tang, *Waste Manag.*, **1993**, *13*, 361.
- [191] Y. Deng, R. Zhao, *Curr. Pollut. Reports*, **2015**, *1*, 167.
- [192] Y. Nosaka, A. Y. Nosaka, *Chem. Rev.*, **2017**, *117*, 11302.
- [193] X. Feng, Z. Du, E. Sarnello, W. Deng, C. R. Petru, L. Fang, T. Li, Y. Li, *J. Mater. Chem. A*, **2022**, *10*, 7896.

- [194] Y. Huang, J. Xiong, Z. Li, Y. Yao, X. Luo, Z. Liang, *Chem. Eng. J.*, **2023**, 471, 144235.
- [195] S. Yin, Z. Li, Y. Hu, X. Luo, J. Li, *Green Energy Environ.*, **2023**, DOI 10.1016/j.gee.2023.03.003.
- [196] A. FUJISHIMA, X. ZHANG, D. TRYK, *Surf. Sci. Rep.*, **2008**, 63, 515.
- [197] S. Tengeler, B. Kaiser, D. Chaussende, W. Jaegermann, *Appl. Surf. Sci.*, **2017**, 400, 6.
- [198] A. Borodin, N. Borisenko, F. Endres, *J. Phys. Chem. C*, **2018**, 122, 5481.
- [199] B. Han, W. Wei, M. Li, K. Sun, Y. H. Hu, *Chem. Commun.*, **2019**, 55, 7816.